MEMS Demodulator Based on Electrostatic Actuator

by

So-Ra Chung

A thesis
presented to the University of Waterloo
in fulfillment of the
thesis requirement for the degree of
Doctor of Philosophy
in
Systems Design Engineering

Waterloo, Ontario, Canada, 2013

I hereby declare that I am the sole author of this thesis. This is a true copy of the thesis, including any required final revisions, as accepted by my examiners.

I understand that my thesis may be made electronically available to the public.

Abstract

This thesis provides analysis and modeling for one of the Micro-Eletro-Mechanical System (MEMS) electrostatic actuator that consists of a micro-plate at the end of a cantilever beam, and introduces different type of MEMS electrostatic actuator; a paddle structure, which is a micro-plate suspended by two cantilever beams on each side. An electrode plate is placed right under the micro-plate to apply an actuation voltage. A step-by-step analysis explains how to obtain each parameter used for the simulations. Static and dynamic models are presented with governing equations for the paddle-shaped MEMS electrostatic actuator. The key findings are that the proposed electrostatic MEMS demodulator architecture taking advantage of the resonance circuit principle not only theoretically work in analytical model, and numerical simulations, but also work in real life. For the Amplitude Modulations (AM) demodulations, simulations with various damping factors are provided, and experimental data are discussed. By measuring the displacement using the phase detector circuit and vibrometer, as a proof of versatility of the demodulation architecture based on the MEMS electrostatic actuator, the results from Frequency Modulations (FM), Amplitude Shift Keying (ASK), and Frequency Shift Keying (FSK) demodulation scheme experiments that are conducted with the physically identical dimensions and configuration are provided. The future plan for further analysis and experiment is discussed at the end.

Acknowledgements

All glory to God, Most Gracious, Most Merciful, Whose bounties and blessings are ever dominating throughout my life.

I would like to express my deep gratitude to my supervisor, prof. John T.W. Yeow for being an invaluable source of resources, growth, and supervision. I would like extend great appreciation to my other professors in committee members; prof. William Melek, prof. Nasser Azad, and particularly for professor Eihab Abdel-Rahman for the tremendous help, encouragement, and guidance.

Thanks are due to my friends and colleagues from Advanced Micro- Nano- Device Lab, SYDE, and ECE department for valuable insights that enriched my work. I always enjoyed the technical discussions I had with fellow students those who are now go by the names; Dr. Forouzanfar, Dr. Khater, Dr. Park, Dr. Wan, Dr. Towfighian, Dr. Logan, Dr. Wang, Dr. Shahini, Dr. Bai, Dr. Ma, and Dr. Sihna.

Many thanks go to the SYDE administrators, especially Vicky Lawrence, for their patience and support in response to all my demand, requests, and questions. I am extending my appreciation to ECTI and CMC for fabrications; and Teaching Assistantship, NSERC and UW president scholarships for the financial privilege and honor.

Finally, my strong appreciation goes to some people who shared every day with me throughout the course of this work. Their support, patience, and understanding played a major role in helping me finish this thesis: my spouse, parents, parents-in-laws, little sister and kids who brought so much joy to my life and who have been a great source of energy and inspiration. No words of appreciation could ever reward them, including the seven who have moved on to the eternal life during this period, for all that they have done for me, especially my cousins and nephew. In the midst of joy and grief, Fr. Joachim Lee made understanding of the life journey and my metamorphic personal transformation possible. I am, and will ever be, indebted to them for all achievements in my life.

Dedication

This is dedicated to wounded travelers yearning for Home.

Glory to God in the highest,

and peace on earth.

Thanks be to God!

Contents

List of Tables

List of Figures

Abbreviations

MEMS	Micro-Electro-Mechanical System
AM	Amplitude Modulation
FM	Frequency Modulation
PM	Phase Modulation
OOK	On-Off Keying
ASK	Amplitude Shift Keying
FSK	Frequency Shift Keying
PSK	Phase Shift Keying
LO	Local Oscillator
PLL	Phase Locked Loop
SDR	Software Defined Radio
BPF	Band Pass Filter
LPF	Low Pass Filter
VCO	Voltage Controlled Oscillator
MMIC	Monolithic Microwave Integrated Circuit
SEM	Scanning Electro Microscope
DETF	Double Ended Tunning Fork

Nomenclature

m	Mass of parallel plate actuator
b	Damping coefficient
k	Spring constant
ϵ	Permittivity of air
A	Area of micro-plate
V_{rms}	Root mean square voltage applied to actuator
$g_\circ$	Initial gap
x	Displacement of micro-plate
L	Inductance
$C_\circ$	Initial capacitance of parallel plate
C_p	Parasitic capacitance of parallel plate
C_m	Capacitance of electrostatic actuator
C_{cap}	Total capacitance
q	Charge stored in parallel plate actuator
f_b	Baseband frequency
f_c	Carrier frequency
ω_e	Electrical resonant frequency
ω_m	Natural frequency
f_{IF}	Intermediate frequency
f_{LO}	Local Oscillator frequency
f_{RES}	Resonant frequency
$f_\circ$	Natural frequency
$f_{primary}$	Primary frequency, f_1
$f_{secondary}$	Secondary frequency, f_2
f_{start}	Start frequency for FSK at resonance
f_{stop}	Stop frequency for FSK at lower frequency

Chapter 1

Introduction

This thesis presents research focusing on development of a new architecture to demodulate the front end Radio Frequency (RF) signal. It uses MEMS electrostatic actuators and interprets the baseband signal as displacement of a parallel-plate electrostatic actuator. The feasibility of this architecture has been studied for both analog and digital modulation schemes. The operating principle of the proposed demodulation device is explained and the analytical modeling and simulation results are presented as well as experimental validation.

Typical RF receivers, Figures 2.3 and 2.4, consist of a front end, a bandpass filter, Low Noise Amplifier (LNA), a local oscillator (LO), and a mixer that recovers the baseband signal from the modulated RF signal. In a heterodyne receiver, there are one or more Intermediate Frequency (IF) stages. In homodyne (direct conversion) receiver, there is no IF stages. The mixer recovers the baseband signal by mixing a signal, with a frequency equal to the carrier frequency, f_c, produced by a local oscillator with the input RF signal.

Recent developments in Micro-Electro-Mechanical-Systems (MEMS) technology have shown the benefits of merging mechanical components within electrical circuits. Interest has thus increased in improving the performance of electrical systems by applying MEMS technology to replace existing electrical components and subsystems.

In the proposed demodulation architecture, the baseband signal is recovered using a MEMS electrostatic actuator. The architecture exploits the fact that the mechanical resonance frequency of the MEMS actuator is much lower than carrier frequency of the RF signal. Further, the frequency of the baseband signal is much lower than the mechanical resonance frequency of the MEMS actuator. As a result, using the input RF signal to excite the MEMS actuator electrostatically, it will respond with a displacement that is linearly proportional to the baseband signal while filtering out the carrier frequency.

MEMS electrostatic actuator, RF modulations schemes both analogy and digital, resonant drive circuits, mechanical down-converting signals, MEMS demodulations, displacement detection using a vibrometer and phase detector are dealt with in this thesis.

Two types of parallel-plate electrostatic micro-actuators were considered for modeling, analysis, and experimental verification. They were used in conjunction with a resonant drive circuit and a phase detector to demonstrate a fully functional demodulator. The results were independently verified using a micro-motion vibrometer. Experimental data support simulation results to show that the realized device is capable of demodulating input RF signals to extract the baseband signal.

1.1 Motivation

There are clear advantages of using MEMS electrostatic actuator as a demodulator for down-conversion compare to traditional methods. This section discusses potential benefits of the proposed MEMS down conversion architecture. Traditionally, a typical receiver takes a modular form consisting of pre-amplifier, low pass filter, mixer, local oscillator, and detector. Each stage requires signal conditioning and careful matching for comparability. Even an ideal mixer, a multiplier, employs nonlinear characteristics of analog circuit. Latest development in Software Defined Radio (SDR) [1] indicates that high linearity in front-end

analog circuit is necessary even for the SDR that pride on the reconfigurability. Low power consumption, good linearity, frequency response accuracy are the desired features[2].

Given similar performance, homodyne down-conversion is superior to heterodyne down-conversion, since it requires less electronics components, thereby offering advantages in cost, size, power consumption, and low frequency $(1/f)$ noise. The main perceived advantage of MEMS down-conversion is the homodyne down-conversion for high carrier frequencies is realizable under this architecture. In fact, the device will even become more efficient and more advantageous as the current trend for increased carrier frequency continues.

Currently, 2.4 GHz WiFi receivers require IF stages. The current homodyne-equivalent technology, requiring no IF stages, is SDR which take advantage of a Digital Signal Processing (DSP) Micro-Processor (μP). This technology requires analog to digital conversion with a sampling frequency at least twice the carrier frequency, $(2f_c)$, and typically ten times that frequency $(10f_c)$. However, there are no 24 GHz Analog-to-Digital converters in the market yet.

The proposed MEMS down conversion architecture requires no IF stages to down convert high frequency signals, in fact its performance will improve as the carrier frequency moves further down the frequency spectrum away from the MEMS actuator's mechanical resonance frequency. On the other hand, it does not preclude the implementation of multiple IF stages in the receiver design should that be required for other purposes, since homodyne mixers can be compounded to implement a heterodyne mixer.

The key benefit of using MEMS demodulator architecture are: multi-mode reconfigurability. The newly developed architecture takes advantage of MEMS electrostatic actuator by combining resonant circuit which was developed [3] for controlling the displacement of a cantilever beam for it to increase the displacement beyond a typical pull-in voltage, and phase detector for displacement detection.

1.2 Research Hypothesis and Statement

Research hypothesis and thesis statements are as the following: it is hypothesized that, when a MEMS electrostatic actuator is excited with a signal consists of mixed frequencies (transmitted modulated signal) sufficiently apart – a lower frequency (information signal) below the natural resonance and a higher frequency (carrier signal) at an electrical resonance – the mechanical response of the moving electrode will follow the lower frequency with magnitude of root-mean-square (RMS) voltage in forms of displacement.

1.3 Contribution

The contributions of this research are:

1. Examined the feasibility of using arbitrary MEMS electrostatic actuators in demodulation device using the proposed MEMS demodulation architecture
2. Developed and realized a fully functional MEMS AM/FM demodulator
3. Developed and validated a MEMS Digital demodulation device

1.4 Thesis outline

This thesis is organized into five chapters. The first chapter outlines research motivations and hypothesis introducing the idea of demodulation using MEMS electrostatic actuators including a brief review on existing state of art MEMS demodulators. Chapter 2, reviews literature dealing with micro-demodulators, mixer-filter, SDR, and mechanical radio in depth. Chapter 3 analyzes the use of MEMS electrostatic actuators for demodulation.

Analytical models of the actuators are presented and the operating principle of the demodulators is explained. The terminology and basic definitions used to describe the performance of MEMS electrostatic demodulators is discussed and their mathematical models have been developed. MEMS demodulation metrics, such as gain flatness, mechanical damping ratio impact on the dynamic range, operational bandwidth of the baseband signal, and electrical quality factor (Q factor) impact on channel selectivity is described. Numerical simulations results are presented. Chapter 4 presents the results of AM/FM/ASK/FSK demodulation experimental verification and validation of MEMS demodulator. Chapter 5 summarizes the contributions of the thesis and points out the challenges that need to be addressed in future work.

Chapter 2

Literature Survey

2.1 Introduction

This section provides a brief overview of RF receiver architectures and demodulation schemes with a particular reference to the proposed MEMS demodulation architecture. It also reviews the state-of-the-art in MEMS devices developed or proposed to replace or supplement traditional demodulators in RF front end.

2.2 Overview of RF Communications Architecture

Since James Clerk Maxwell proved the existence of the invisible electromagnetic wave, in 1887, and Guglielmo Marconi achieved radio communications across the English Channel, in 1899, wireless transceivers has become an omnipresent commodity. Receivers are used in the RF communications to resolve the baseband signal (information content) out of an incoming RF signal. A typical RF receiver consists of an antenna (ANT), a band-pass filter (BPF), a low noise amplifier (LNA), a local oscillator (LO), and a mixer that recovers the

baseband signal from a modulated RF signal. The main focus of this project is the mixer part of the receiver, therefore the front end –antenna, band-pass filter, low noise amplifier– and packaging of the overall device are not dealt with.

For demodulation, the RF signal is multiplied by the carrier signal to reproduce the original baseband signal. In a heterodyne receiver there is more than one intermediate frequency stage between the RF and the baseband signals. In a homodyne receiver, referred to as a 'direct convert' receiver, the input RF signal is directly converted into the baseband signal [4]. Heterodyne receivers are the most commonly used among wireless transceivers. Although they have good sensitivity and selectivity, homodyne receivers obviously not only take up less hardware but also use less power and occupy smaller area, since they uses one mixer less than heterodyne receivers and a low-pass filter (LPF) instead of a narrow-band, high-Q, bandpass filter. Before dealing with the receiver architecture in detail, terminology of modulations schemes are explained in the following section.

2.2.1 Analog Modulation

In analog modulation, the information content of the baseband signal, such as human voices in electrical form is mixed with a carrier frequency as shown in Figure 2.1 determines the carrier signal characteristics. For audio content, the baseband frequency ranges from 20 Hz to 20 kHz. The carrier frequency, f_c, for amplitude modulation (AM) broadcasting in the Americas, which belongs to the International Telecommunication Union (ITU) region 2, ranges from 535 kHz to 1605 kHz. Every 10 kHz bandwidth in the frequency spectrum from 540 kHz to 1600 kHz is assigned for an AM broadcasting channel. The carrier frequency f_c for FM broadcasting ranges from 88 MHz to 108 MHz. The baseband signal contains the same audio information content for AM and FM modulations. For the AM communications, the amplitude of the carrier varies in accordance with the baseband signal.

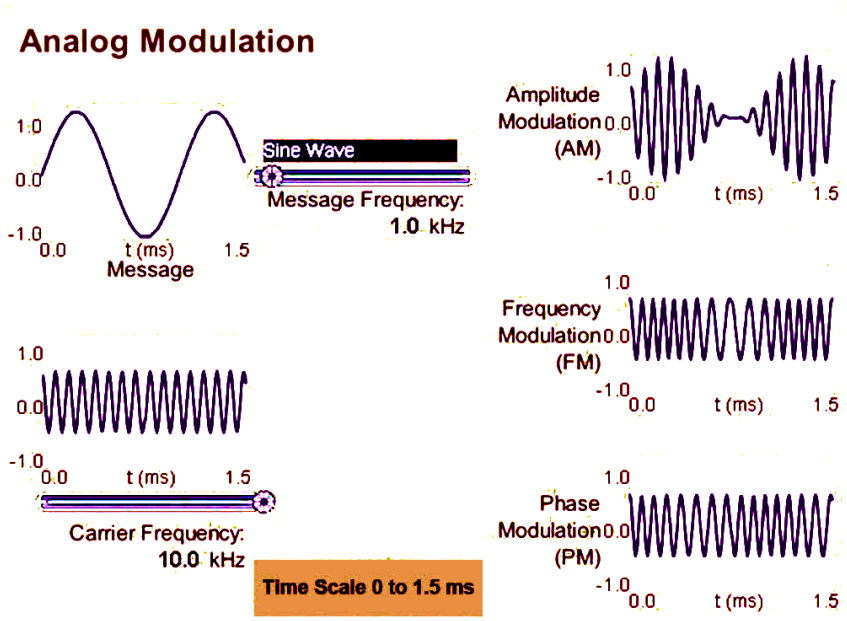

Figure 2.1: Analog modulation: Input baseband and carrier signals and output amplitude modulated, frequency modulated, and phase modulated signal samples

A Modulating signal, $m(t)$, is given by

$$s(t) = Re\{g(t)e^{j\omega_c t}\} \tag{2.1}$$

a complex envelope $g(t)$ is function of the modulating signal $m(t)$.

$$g(t) = f[m(t)] \tag{2.2}$$

The baseband signal is multiplied by AM carrier signal and the envelope of the mixed output signal follows the baseband signal

$$f[m(t)] = A_c[1 + m(t)] \tag{2.3}$$

$$m(t) = A_m e^{j\omega_m t} \tag{2.4}$$

The frequency of the output signal varies linearly with the amplitude of the baseband signal within a pre-defined range around the carrier frequency f_c. ω_c is $2\pi f_c$. A_c is amplitude of the modulated carrier signal. ω_m is $2\,\pi f_m$. One f_m at a time is chosen for simulation

and experiment, but theoretically any frequency below natural frequency of actuator can be used.

$$s(t) = e^{j\omega_c t} \tag{2.5}$$

Thus, the mixed FM output signal has a higher frequency when the baseband signal amplitude is high and a lower frequency when the amplitude is low. In phase modulation (PM), the phase of the carrier signal varies in accordance with the input baseband signal. PM is not explored in this thesis.

2.2.2 Digital Modulation

In digital modulation, the information content of the baseband signal, such as human voices, is first discretized then used *discretely* to adjust the carrier signal characteristics. Digital modulations benefit from higher reliability, higher data rates, and better immunity to noise than analog modulations. On-off keying (OOK), amplitude shift keying (ASK), frequency shift keying (FSK), and phase shifting keying (PSK) are typical examples of common modulation schemes that vary the amplitude and/or phase of a carrier signal in a discrete manner at a discrete time by mixing a series of binary digits with the carrier wave. Figure 2.2 shows three different types of digital modulation schemes.

For ASK modulation scheme, when the binary digit is zero, the amplitude of the modulated signal is small compared to the amplitude of the modulated signal for binary digit one. Therefore, the discrete state of the amplitude of the RF signal has a direct correspondence with the on-off (one-zero) state of the digital signal. For FSK, when the binary digit is zero, the frequency of the modulated signal is set to discrete frequency lower than f_c. Conversely, frequency of the modulated signal is set to a discrete frequency higher than f_c for binary digit one. The 'high' and 'low' frequency states, therefore, correspond to the zeros and ones of the digital signal. For PSK, the amplitude and phase stay the same as

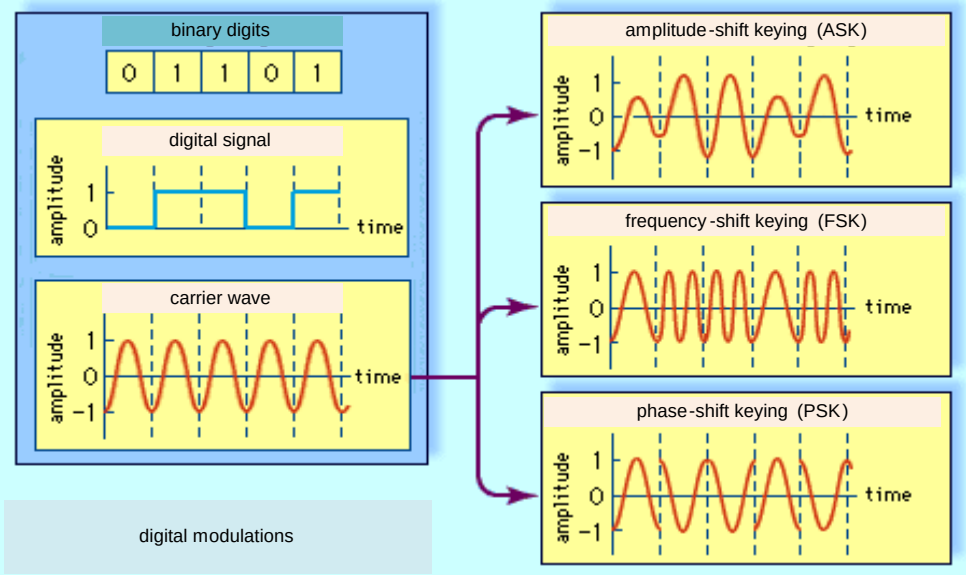

Figure 2.2: Digital modulations illustration for ASK, FSK, and PSK

those of the carrier signal for binary digit zero but the modulated signal is out of phase, showing a 180° shift with respect to the carrier signal, when the binary digit turns to one.

More advanced types of digital modulations include binary phase shift keying (BPSK) with one bit, quadrature phase shift keying (QPSK) with four discrete states or two bits for the shift phase, quadrature amplitude modulation (QAM) with both discrete amplitude and phase combinations, Gaussian minimum shift keying (GMSK) with spectral efficiency and resilience to noise, and orthogonal frequency-division multiplexing (OFDM) with multiple channels operating in the vicinity of one another without interfering with each others signal integrity. Further details of how each modulation scheme works can be found in the many text books on digital communications.[5] This thesis explores simple digital demodulations first. Thus verification of using MEMS demodulator for the more advanced types of digital modulation scheme is out of scope of this thesis.

2.3 Receivers

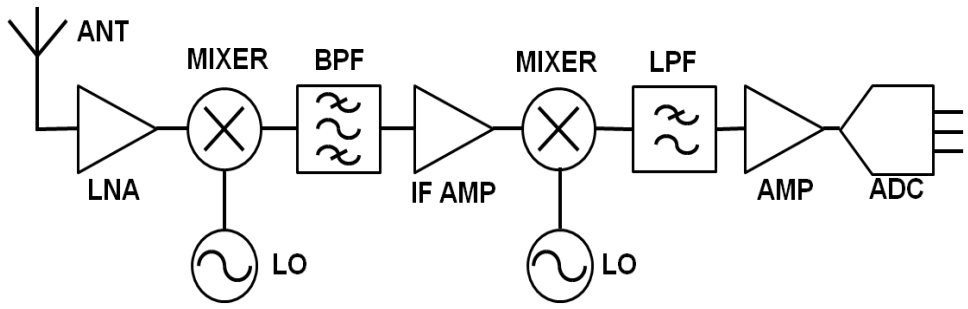

Figure 2.3: The block diagram of a heterodyne receiver

The heterodyne receiver shown in Figure 2.3 converts input signal to an intermediate frequency and then to the baseband signal. The word, hetero, originates from the fact that the receiver takes more than one stage to down convert the RF frequency to the baseband frequency. The IF signal is amplified before further down-converting to the baseband signal. This process provides flexibility in changing the receiver frequency since the rest of the RF receiver components stay the same, except for the frequency of the local oscillator at the intermediate mixer stage.

A known complication in mixing is the appearance of an image frequency. When the received RF or IF signals are mixed, the multiplication of the RF or IF signal at $(f_b + f)$ with the local oscillator signal at f produces two components in the frequency spectrum at the sum and the difference of those frequencies, namely f_b and $(f_b + 2f)$. Of the resulting two frequencies, the component with a frequency further away from the baseband signal is not desired $(f_1 + 2f)$. Thus, an additional filter is needed to reject the unwanted image frequency.

A homodyne receiver is illustrated in Figure 2.4. This receiver is also called a direct convert receiver because it converts the input signal directly into the baseband signal with no intermediate frequency stage [4]. There are definite advantages associated with having

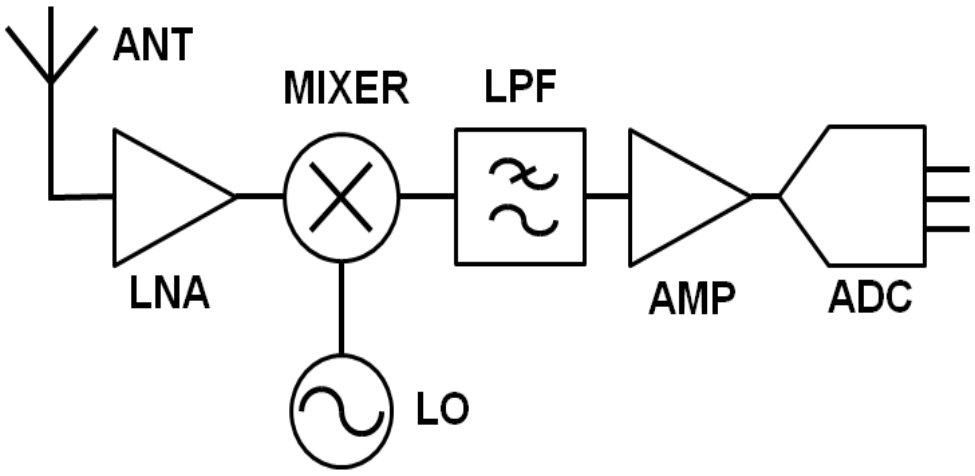

Figure 2.4: The block diagram of a direct conversion homodyne receiver

less hardware, such as cost and size reduction on the overall receiver. Moreover, there is one less mixer than in a heterodyne receiver. Further, a homodyne receiver uses low pass filtering instead of high-Q, narrow bandpass filtering.

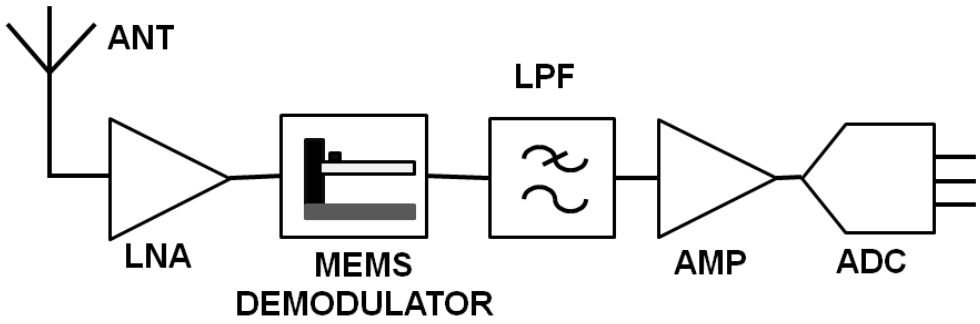

Figure 2.5: A block diagram for a direct conversion homodyne receiver employing a MEMS demodulator

This research effort seeks to replace the discrete electrical components constituting the mixer and local oscillator in a homodyne receiver with a MEMS-based demodulator. Figure 2.5 shows a block diagram of the modified homodyne receiver where a MEMS demodulator has been used to replace the mixer-oscillator stage. While, in essence, it is

possible to replace mixer-filter combinations in heterodyne receivers with similar MEMS demodulators, we restrict our interest to homodyne receivers since it proves the concept for both classes of receivers. Further, as noted above MEMS demodulators constitute a unique enabling technology to implement direct conversion homodyne receivers for high frequency RF signals.

2.4 RF MEMS and MEMS Mixer

MEMS was developed based on the infrastructure of silicon fabrication technology. It is capable of integrating multiple functions in RF communication circuits. The main advantage of MEMS is that they integrate moving parts with Integrated Circuits (ICs). MEMS inductors and capacitors are smaller than their equivalent off-chip passive components. MEMS filters and phase shifters are known for their low loss high-Q characteristics compared to their IC equivalents. MEMS switches have relatively low insertion loss and high off state isolation compared to solid-state switches. Over a broad frequency range, MEMS components have better linearity compared to their solid-states counterparts. Tunability, reconfigurability, and low power consumption are other advantages of MEMS.

Indeed, many receiver stage components have been replaced with MEMS parts in the last decade. Figure 2.6 identifies components that were targeted in 1999 [6] as replaceable with the MEMS components. Currently, state-of-the-art efforts are target improvement of individual components especially realization of high-Q filters for selectivity. There has been continuous development in the past ten years towards portable wireless communication devices and micro mechanical radio driving efforts to realize MEMS switches, varactors, inductors, micro-machined transmission lines, resonators, thin film bulk acoustic resonators (FBARs), filters, antennas, etc... Many of these components and systems are designed to be tunable.

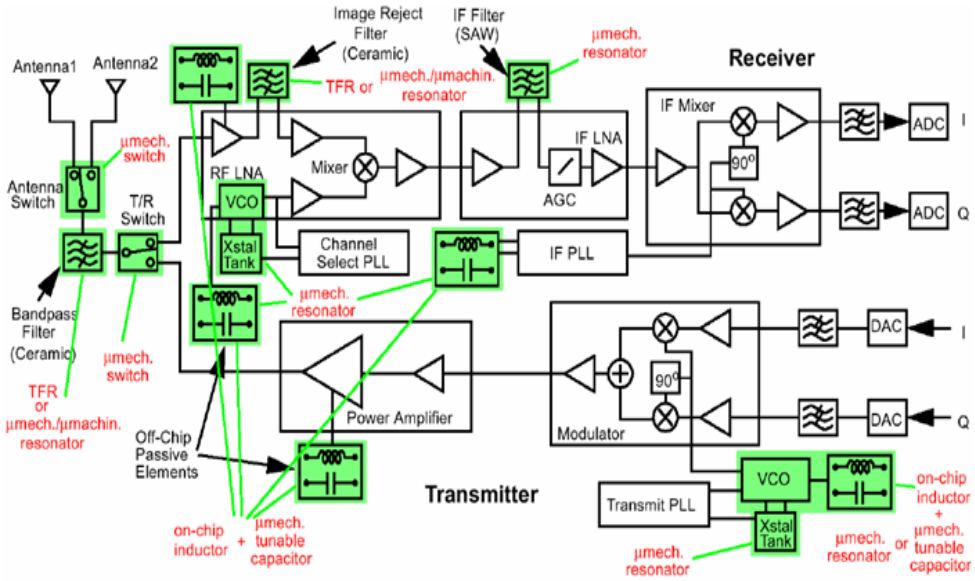

Figure 2.6: Proposed MEMS replacements for wireless transceiver components[6]

Table 2.1 presents a list of RF elements and systems for the receiver stage that are implemented with IC and MEMS technologies. Still, integrating each component in one chip is challenging [6] [14][9][15]. There has been miniaturization effort combining stages of transceiver architecture. For example, Wong and Nguyen's 'mixler' is a combined mixer-filter that serves as ab RF-to-IF voltage transfer function employing two bridge-like fixed-fixed beam micro mechanical resonators coupled by a non-conductive beam [13]. This design was further enhanced by Koskenvuori and Tittonen [12] who introduced parametric amplification by driving the mixer at twice its natural frequency, thus improving the conversion efficiency.

2.4.1 MEMS Mixers

In this subsection, existing RF MEMS mixers and their operational principles are discussed. Mixing two signals can be done intrinsically and extrinsically. Brown[16] has identified

Table 2.1: Typical wireless front-end components replaced with IC/MEMS

Stage	Typical Component	IC/MEMS
Antenna	Physically large antenna	Micro machined antenna [7]
Switches	Electromechanical, solid state, field effect transistors (FET), diodes	RF MEMS switches [8][9]
Filters	Parallel and series resistors, inductors and capacitors	RF MEMS tunable filters [10]
LNA	Transistors	Monolithic-microwave-integrated-circuit (MMIC) and Gallium arsenide (GaAs) FET [11]
Mixer	Diodes or transistors	MEMS mixer [12]
LO	Quartz crystal oscillators, LC/RC oscillators, and Voltage-controlled oscillators (VCO)	MEMS resonator [13]

three classes of RF MEMS depending on the relationship between the function of the MEMS structure and its location with respect to the RF circuit:

- extrinsic: if the structure is located outside an RF circuit controlling other devices,
- intrinsic: if the structure is located inside the RF circuit but decoupled from its actuation signal, and
- reactive: if the structure is inside the RF circuit and coupled to the actuation [8].

Adopting this terminology, we classify MEMS mixers depending on the entry location of the primary signal, $f_{primary}$, in relation to the secondary signal, $f_{secondary}$. Throughout this thesis, where two distinguished frequencies – for example, an RF information signal along

the carrier frequency, f_1, and a local oscillator frequency, f_2 – enter the MEMS mixer via two mechanically separate input ports it is defined as an extrinsic mixer. Where all input signals enter the MEMS mixer via one input port, it is termed an intrinsic mixer. The word 'mixer' is loosely used interchangeably with "mixer-filter". If the MEMS structure, often a resonator, is capable of selecting a specific range of frequencies, the word "filter" is added [17]. Further we distinguish two main types of MEMS mixers: electrostatically actuated electro-mechanical mixers and thermally actuated electro-thermal mixers.

Electro-mechanical Mixing

The structure and operation of an electro-mechanical mixer is illustrated in Figure 2.7. The mixer-filter of Wong and Nguyen is made of two identical resonators, depicted in blue, connected by a highly resistive coupling beam, depicted in yellow. The size of the each resonator is $18.8 \times 8 \times 2.1\mu$m. The resonators vibrate up and down in the z-direction when the carrier signal is applied to the RF input electrode, depicted in red, and the local oscillator signal is applied via the anchors at both ends of the input resonator. The reported resonance frequency is $\omega_\circ = 37$ MHz which is equal to the desired intermediate frequency, ω_{IF}. This mixer-filter requires a 200 MHz local oscillator input. The reported capacitor gap between the resonator and the input/output electrodes is 32.5 nm. The ratio of the beams thickness to the air gap is 65:1, which ensures a very high electro-mechanical coupling coefficient. The air gap was reduced to one-third of that reported in a previous work [18] in order to improve electro-mechanical coupling.

The RF mixing principle is based on electrostatic actuation. The electrostatic force exerted on the beam pulls the resonator toward the bottom electrodes. The RF signal applied to the centre electrode ranges from 233 MHz to 242 MHz. It is mixed with the LO signal. The output of the two mixed signals is in the range of 33 MHz and 42 MHz, and peaks at 37 MHz, which is the desired intermediate frequency. Frequency tuning is enabled

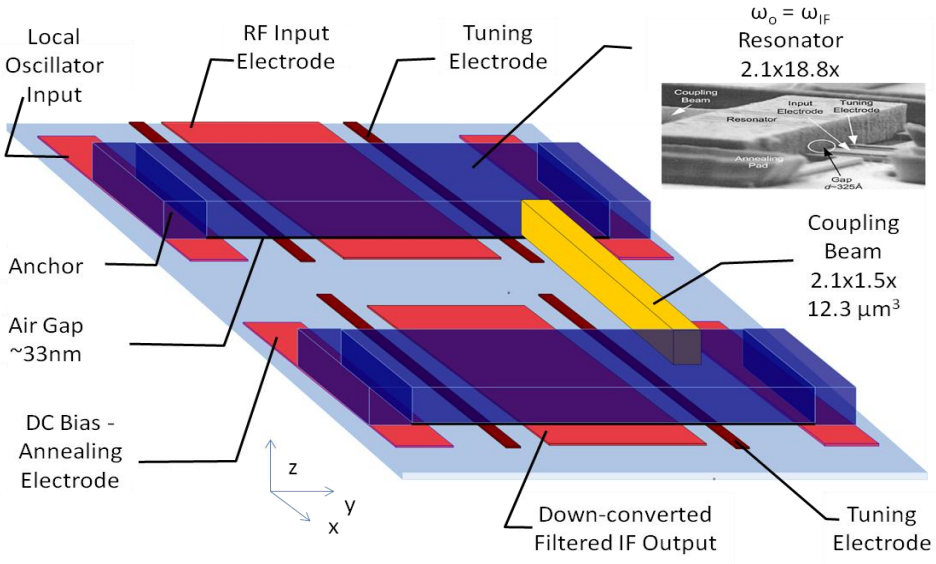

Figure 2.7: Schematic diagram of 200 MHz to 37 MHz down-converting MEMS mixer-filter [19]

by two electrodes on the both sides of the bottom centre electrode as shown in Figure 2.7. The DC bias annealing electrode is required for the output resonator to transducer the resonator motion into the output IF signal. The reported conversion loss and insertion loss are 13 dB. The *through* measurement is -72 dBm, and the mixer output is 85 dBm while the noise floor is -100 dBm. The key features to note are the resonator dimensions, which are designed to obtain the output frequency of the mixer-filter. The output frequency is the IF centre frequency in the case of a heterodyne receiver, and the baseband frequency in the case of a homodyne receiver. The RF frequency is fed via electrode, and the local oscillator frequency via the anchors. The device features two input sources. The output signal is sensed by the down-converted filtered IF output electrode. The fabrication process is rather complex. It leaves etch-byproduct residues on the poly-silicon (poly-Si) electrode, which is only 40 *n*m away from the structural poly-Si. The non-conductive capacitive coupling beam requires a quick thermal-annealing process. This mixer-filter is termed here

as an extrinsic mixer since it requires two separate input signal ports.

Micro-Electro-Mechanical Parametric Mixing

Frequency conversion performance has been improved by Koskenvuori and Tittonen. Figure 2.8 is a 3-D reconstruction of a scanning electron microscopic (SEM) image of their mixer-filter [1, 17-20]. It takes advantage of parametric resonance of two double-ended tuning forks (DETFs) depicted in blue in the Figure 2.8. The RF input, the LO input, and the IF output electrodes are depicted in red blocks. The mechanical coupling beam, depicted in yellow, similar to that in previous work by Wong and Nguyen [19], isolates the IF output from the RF input. It is worth noting that the local oscillator signal is directly applied to the input DETF structure transversely via a 170 nm coupling gap.

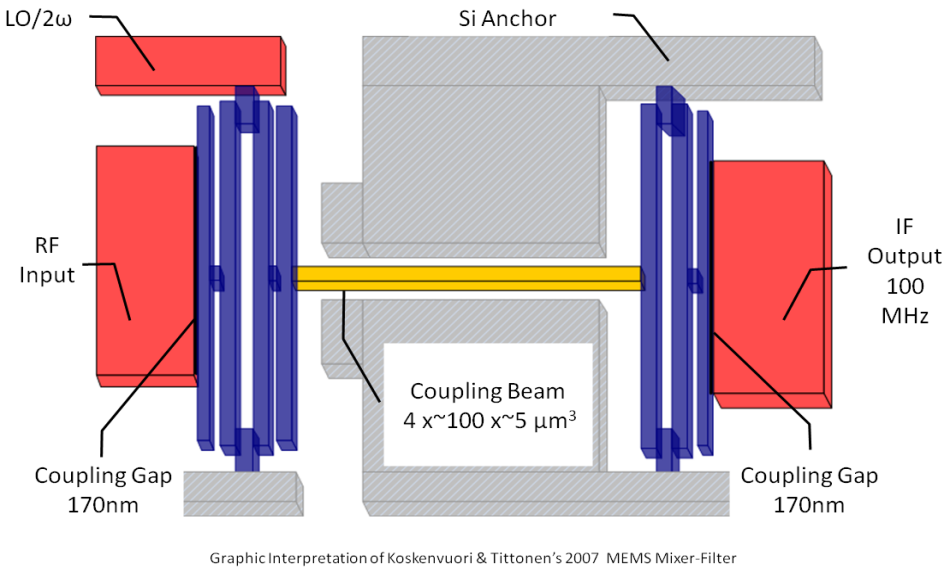

Figure 2.8: Schematic diagram of DETF type MEMS Mixer[19]

The input carrier frequency, f_c , is 500 MHz, resonance frequency, $f_\circ$ ($=f_{res}=f_{IF}$) is 1.338 MHz, and the local oscillator inputs f_{LO}s are 10 MHz ,100 MHz, and 390 MHz.

Koskenvuori and Tittonen's 2008 work reports conversion performance improvement by reducing the coupling gap from 170 nm to 100 nm. They presented the above structure in four different papers submitted in early 2007 [20][12][21][22]. Overtone excitations of the micro resonator is conducted for nonlinearities test. The excitation takes local oscillator frequencies of 10 MHz, 100 MHz, 390 MHz and mixes them with the resonant frequency of 1.338 MHz resulting in RF frequencies of 11.338 MHz, 101.338 MHz, and 391.339 MHz respectively. The ratios of the voltage output to the voltage input were compared in terms of conversion loss, which is one of design criteria for the MEMS demodulator described in the next chapter. GHz-range FSK-reception with MEMS resonators [20] presents a down-conversion method which was tested with carrier frequencies of 0.5 GHz and 1.5 GHz. The side band is specifically chosen to match the difference between the carrier frequency. A sideband is that is close to the resonator's first eigenfrequency is chosen to be first sideband and another sideband which is further away from the carrier frequency is chosen to be the second sideband which takes the second eigenfrequency of the same resonator. Such a mixer requires no local oscillator. This group's latest paper [22] presents results from exciting the device at twice the resonance, 2 ω_0; thus they introduced the term, *parametric resonance* or *parametric amplification*. The spring constant term, k, includes modulated amplitude of the spring constant excited at the 2 ω_0. For example, when the RF electrode is coupled to 0.5 GHz input, the output, the IF electrode, reads 1 MHz.

Micro-Electro-Thermal Mixing

Micro-electro-thermal mixing is another method of signal mixing. Figure 2.9 illustrates a Poly-Si dome shape resonator employed by Reichenbach *et al.* [23] to implement a mixer. The advantage of electro-thermal actuation over electrostatic actuation is that it does not require the fabrication of nanometer capacitive gap. The diameter of the dome is about 30 μm. When RF signal is applied to a gold thin-film resistor with 250 mV DC bias,

the Joule heating causes the out-of-plane deflection. When the AC current through the micro heater matches the resonator frequency, the heat is modulated and dissipated at the compatible rate as the mechanical resonance since the resonator has smaller thermal mass and thus a smaller time constant. The quality factor, Q, varies between 3000 and 10000 in vacuum but in the air it is about 100. The resonance frequency, f_{res} is 12.7 MHz which is purposely matched to the mechanical resonance.

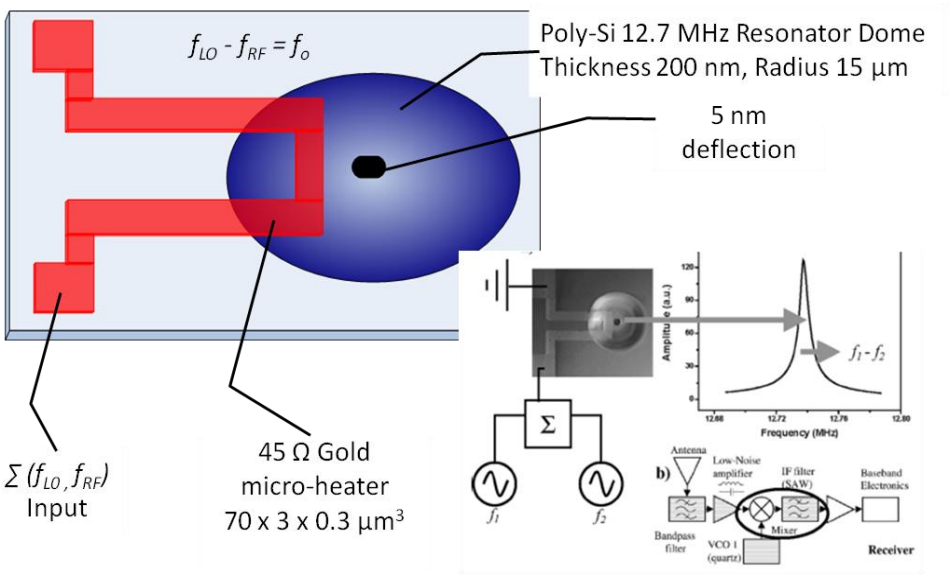

Figure 2.9: Thermal MEMS mixer-filter [23]

The local oscillator frequency is set at 60 MHz. The input to the resonator is the sum of the chosen carrier frequency, f_c at 72.7 MHz and the Δf and 2Δf, where Δf is swept from 20 kHz to 500 kHz. This configuration takes advantage of two tones offset from the carrier frequency for the test signals. The key is that the gold resistor acts as the frequency translator and the coupled resonator works as a post mixing filtering. This type of configuration is an example of intrinsic mixing.

One 70 μm by 3 μm gold strip on the resonator serves as a micro heater and another identical size strip acts as a piezoresistor implanted in the resonator [24]. It is an im-

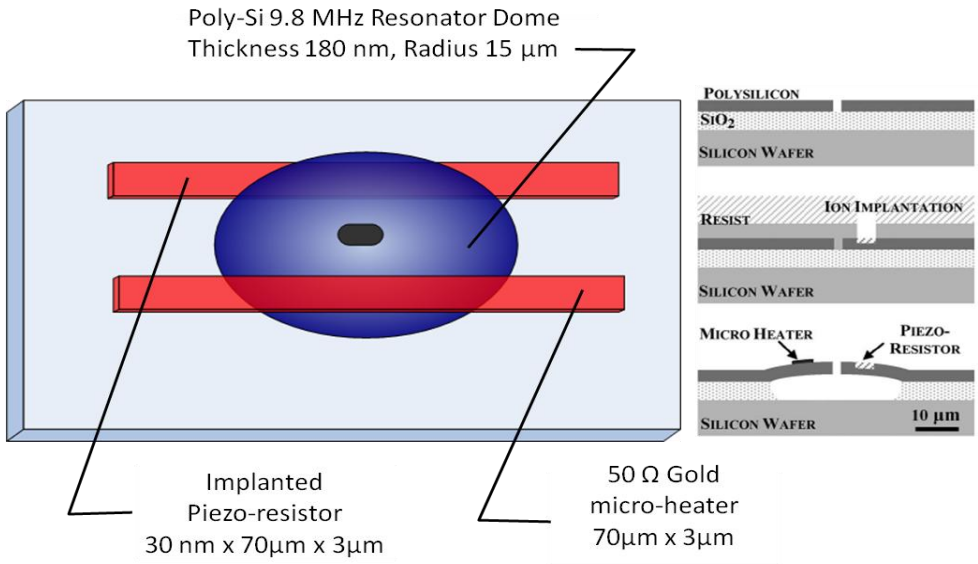

Figure 2.10: MEMS oscillator with integrated resistive transduction [24]

provement from their previous work. The membrane deflection causes strain on the doped silicon strip. The change of the resistance is proportional to the corresponding stain. For the same -20 dBm drive, the inband insertion loss is improved from -65 dB to -35 dB when the resonator is coupled to an operational amplifier.

Figure 2.11 shows the most recent work on MEMS thermal mixer that takes advantage of thermal expansion property of a bimorph resonator [25]. Aluminum strip deposited on the Silicon Carbide in a cantilever beam structure shows the maximum vibration amplitude of 62 nm at resonance of 944.49 kHz when two frequencies of f_1 at 1200 kHz and f_2 at 255 kHz are applied to the two independent aluminum electrodes on top of the silicon-carbide cantilever beam. The f_1 is fixed and f_2 is swept to find the resonance frequency by varying the difference between the two signals in 10 kHz interval. Figure 2.11 a graphical interpretation show the 50 μm long cantilever beam thermal actuator of Mastropaolo et al. Another case of 200 μm long cantilever beam has lower resonance of 89.37 kHz for the similar testing setup. The work reported that there was no more vibration beyond the

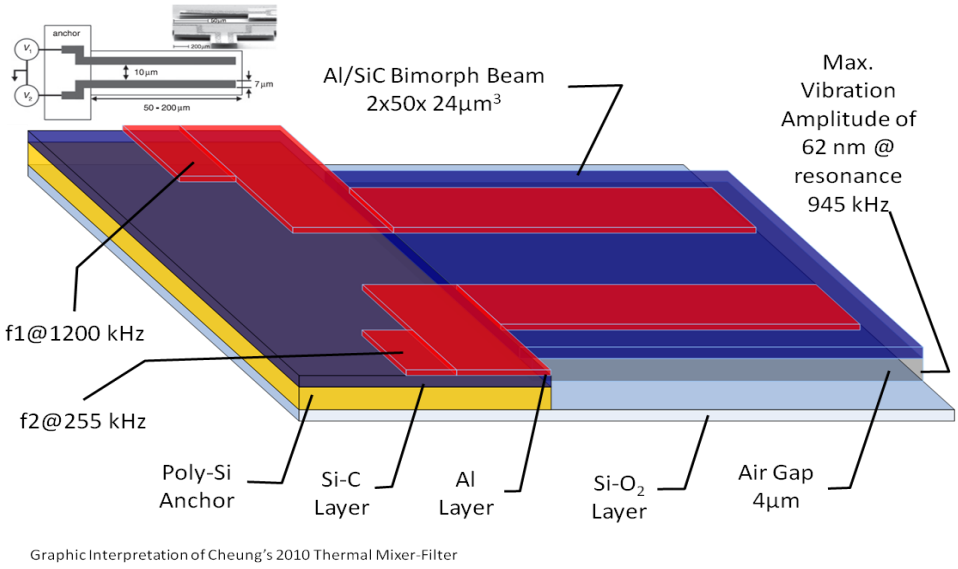

Figure 2.11: Extrinsic electro-thermo-mechanical mixing of two AC voltages [25]

mechanical resonance of the structure.

2.5 Displacement detection

The RF demodulator implemented with MEMS devices exhibits promising performance characteristics such as low power consumption and low noise level. However, in order to physically extract the baseband signal from the modulated RF signal, we need a way to measure the displacement of a MEMS device, which can be any of a cantilever beam, a cantilever beam with attached plate, a fixed-fixed microbeam or even a tethered microplate. Currently, there are three popular displacement sensing methods for MEMS applications: capacitive sensing, piezoresistive sensing and piezoelectric sensing. Each sensing mechanism can be built and implemented on a bulk silicon substrate.

The obvious challenge is in the method of sensing displacement effectively while minimizing the added footprint[20],[12],[21],[22]. Work of [19] measures the signal by capacitive

coupling, and work of [24] integrates piezoresistive sensing method, [23] and [25] use optical methods such as a probe station and a vibrometer. Optical sensing is not a favorable as other methods especially for a portable device such as a low-power wireless communications system. It is widely used for feasibility studies. At the end of a product design, integrated displacement sensing is essential for marketability. The criteria for choosing the most suitable displacement sensing method are as followings: compatibility and easiness of fabrication: maximum sensitivity for small change: dynamic range of displacement measurement, and minimum impact on the existing structure. First, differential capacitive sensing [26] measures the motion of a central movable plate against fixed plates. It requires low actuation driven by voltage driving circuitry to sense high speed charge and discharge the measurement cells. The reported strain sensitivity [27] is 5 mV/$\mu\epsilon$, and the device is vulnerable to sticking phenomenon. Second, piezoelectric sensing [28][27][29] measures the voltage change caused by the change in displacement its strain sensitivity is 5 V/$\mu\epsilon$. The piezoelectric sensing method requires no external circuitry to drive when there is no incoming signal. Its disadvantage is that, at steady-state, when there is no more movement, an absolute displacement is not detectable. Random polarization requires exposure to a strong electric field at an elevated temperature, which may damage the existing structure. Third, piezo resistive sensing [30][29] measures the change of resistance that is proportional to the change of displacement by measuring current. It drifts with temperature, requires external driving circuitry, and consumes power when there is no incoming RF signal. There are advantages to piezoresistive sensing. The strain sensitivity is 0.1 mV/$\mu\epsilon$, and is linearly proportional to the change in the strain in the elastic region. It is easy to deposit piezoresistive material on bulk silicon, for example, a typical gauge factor for Poly-silicon is -30 to 30.

2.6 Summary

In this chapter, literature survey presented the past trend and current state of art MEMS demodulators and defined electrostatic actuation and thermal actuation intrinsic and extrinsic mixers working as demodulator (frequency stepping down). The resonators play an important role in frequency conversion. Most of the cases, it starts from the known mechanical resonance of the structure and move backward on applying appropriate input frequency to determine the performance of the mixer-filters. If the mechanical resonance was initially unknown as in the case of [25], the primary input frequency is swept to find the peak which shows the strongest signal strength. The displacement is assumed to be one-third of the published air gap [20][12][21][22][19] unless they are spelled out [25][24]. The conversion loss in dB is used loosely across literatures. The reported values mean slightly different thing in each literature. For example, 13 dB in [19] includes both conversion and insertion loss whereas the 70 dB in [21] is for conversion loss only. The huge difference in the conversion loss depends on the coupling and efficiency [12]. Since the micro-electro-thermal mixers are not a full mixer-filter circuit integrated systems, the displacement is optically measured. Thus the conversion loss is calculated based on ratio of the output power and input power graph for [23], and the ratio of the maximum vibration amplitude over the minimum detected vibration for [25].

Chapter 3

Modeling and Simulation of MEMS Demodulators

3.1 Modeling of Demodulators

As per the proposed architecture, a MEMS demodulator is composed of an electrostatic MEMS actuator driven by a resonant drive circuit and detected by a phase-detector. Two types of electrostatic actuators are considered in this work:

- a paddle actuator made of a parallel-plate capacitor supported on either side by a micro beam and
- a plate actuator made of a parallel-plate capacitor supported by a cantilever micro beam.

Both actuators were developed for an unrelated research effort [31]. They are used to realize the MEMS demodulator to demonstrate the proposed demodulator independence of the specific characteristics of the MEMS actuator.

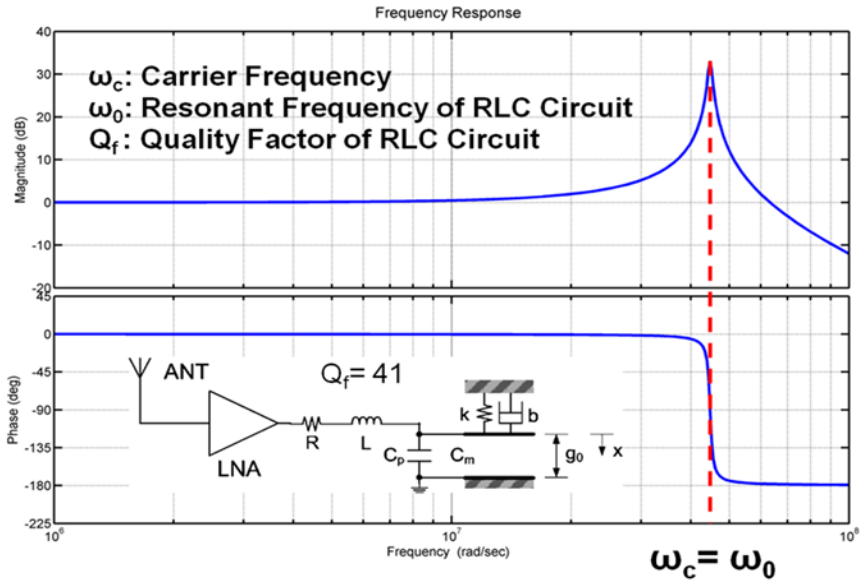

Figure 3.1: Resonance circuit for AM demodulation

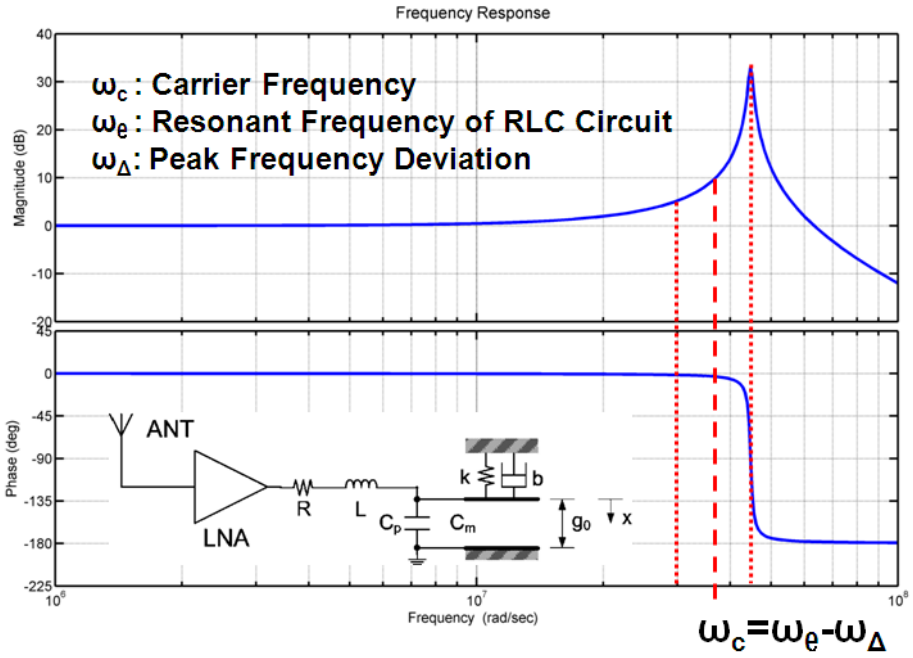

Figure 3.2: Resonance circuit for FM demodulation

The resonant drive circuit shown in Figure 3.1 is made by connecting a commercial discrete inductor, L, in series with the electrostatic MEMS actuator, acting as a variable capacitor, C_m, where the subscript m indicates a moving part. The capacitance of the MEMS actuator depends on the displacement of the micro-plate when the actuation voltage is applied. Parasitic resistance R appears also in series with the inductor and the capacitor. Parasitic capacitance, C_p, appears also in the MEMS actuator and is parallel to the actuator, the variable capacitor. Since the capacitance is predetermined by the size of the micro-plate and capacitor gap of the fabricated actuator, the inductor, L, is the only option we can use to set the electrical resonance frequency, ω_e, to be equal to the carrier frequency, ω_c, in the proposed MEMS demodulator. The electrical resonance frequency is measured experimentally by sweeping the frequency of the input (RF) signal to the resonant drive circuit at a constant amplitude, while monitoring the oscilloscope to record the maximum amplification of the output (actuation) voltage.

In AM demodulation, Figure 3.1, the carrier frequency of the RF signal ω_c is set equal to the natural frequency of the resonant drive circuit $\omega_\circ$ when the actuator is at rest. FM demodulation adopts a similar principle to that of AM demodulation, Figure 3.2 using the same electrostatic actuator. The only difference is that the carrier frequency ω_c is allowed to vary around the electrical resonance frequency $\omega_\circ$ within a range called the peak frequency deviation ω_Δ, such that: $|\omega_c - \omega_\circ| \leq \omega_\Delta$.

3.2 Micro-Actuator Type I: The Paddle Actuator

This section addresses the use of a paddle actuator as a demodulator. The paddle actuator is made of a micro-plate suspended by one cantilever beam on each side. The rigid plate which is suspended equidistant from the two fixed-ends is actuated by an electrostatic force that has been applied via a voltage difference between the plate and a fixed electrode

underneath. The suspended micro-plate is shown in Figure 3.3. Our MEMS demodulation architecture takes advantage of the micro-plate's vertical displacement and assumes that the plate remains parallel to the fixed electrode(substrate) throughout motion. We assume that the anchored ends of the beams are fixed-ends. We also assume that the ends attached to the plate is guided-ends for boundary condition since the plate appears to move freely along the vertical axis. Since the geometry of the micro-structure is symmetrical, we can consider one-half of the structure only. The boundary condition of the fixed-end prevents the beam from translation and rotation, while the guided-end boundary condition just prevents its rotation. In the subsections, static analysis is carried out to figure out the pull-in voltage and range of useful displacement to avoid pull-in instability region; and dynamic analysis is carried out to determine the behaviour of the electrostatic actuator: such as how damping coefficient and and inertia would affect the actuator.[32]

Based on the Euler-Bernoulli beam theory, the beam displacement towards the bottom electrode $w(x)$ is governed by the differential equation

$$EI\frac{d^4w}{dx^4} = q(x) \tag{3.1}$$

where E is Young's Modulus and I is the second moment of area. For the rectangular cross-section beams used in here, the moment of area is

$$I = \frac{bh^3}{12}, \tag{3.2}$$

where h is the thickness of the beam and b is the width of the beam. $q(x)$ is the distributed transverse load applied to the beam. Since the support beams are free of transverse loads ($q(x) = 0$), we can write:

$$w(x) = C_1x^3 + C_2x^2 + C_3x + C_4. \tag{3.3}$$

Third order polynomial is selected to characterize the deflection profile of $w(x)$ since the third derivative of $w(x)$ is proportional to the internal shear $V(x)$. The first derivative of

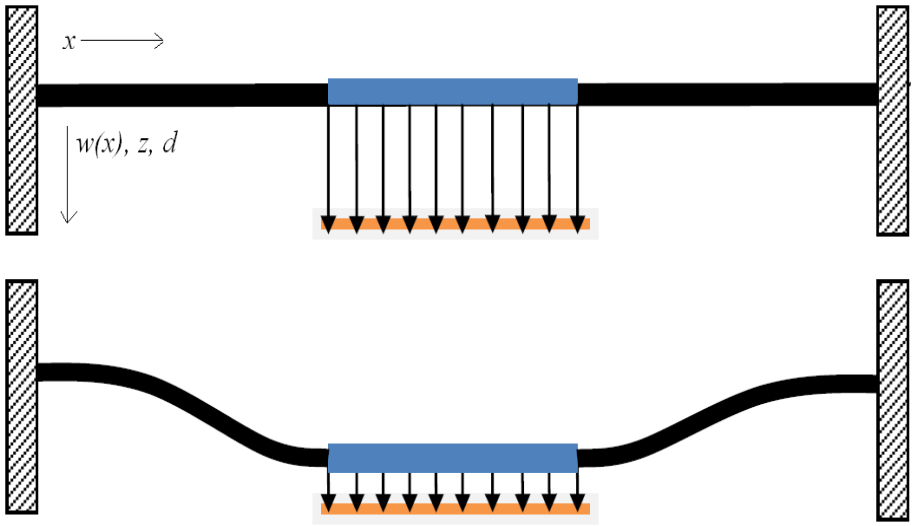

Figure 3.3: The initial and final positions of the paddle actuator subject to a uniform electrostatic force applied to the bottom of the micro plate

$w(x)$ is the slope of the beam:

$$w'(x) = \frac{dw}{dx} = 3C_1x^2 + 2C_3x + C_3. \tag{3.4}$$

where the prime denotes a derivative with respect to the axial position x. The second derivative of $w(x)$ is proportional to the internal moment $M(x)$ in the beam:

$$w''(x) = 6C_1x + 2C_2 = -\frac{M(x)}{EI}. \tag{3.5}$$

Although constant value, EI, is typically included in the $M(x)$ term, EI is carried on to the next equation for its visiblity. The third derivative of $w(x)$ in the beam:

$$w'''(x) = \frac{dM(x)}{dx} = 6C_1 = -\frac{V(x)}{EI}. \tag{3.6}$$

The static deflection problem of the beam can be formulated as deflection under half of the total electrostatic force applied as a point load at $x = L$. We let the left end of the micro actuator act as the origin of x-axis. Since displacement and slope vanish at the fixed-end, we write the boundary conditions there as follows:

$$w(0) = 0 \quad \Longrightarrow \quad C_4 = 0 \tag{3.7}$$

and

$$w'(0) = 0 \quad \Longrightarrow \quad C_3 = 0. \tag{3.8}$$

The right end of the beam ($x = L$) is a guided-end, where the slope vanishes, therefore we can write

$$w'(L) = 3C_1L^2 + 2C_2L = 0 \tag{3.9}$$

The shear force at the guided-end is equal to half of the total force acting on the micro-plate F. Using Equation 3.6, at $x = L$, we can calculated C_1

$$w'''(L) = 6C_1 = -\frac{V(L)}{EI} = -\frac{F}{2EI} \tag{3.10}$$

From Equations 3.9 and3.10, the constants C_1, and C_2 are calculated as:

$$C_1 = -\frac{F}{12EI} \quad \text{and} \quad C_2 = \frac{LF}{8EI}. \tag{3.11}$$

Substituting in Equation 3.3, we obtain the static deflection of the micro actuator in closed-form

$$w(x) = -\frac{F}{12EI}x^3 + \frac{LF}{8EI}x^2. \tag{3.12}$$

The displacement, d, of the micro-plate is equal to the displacement of the micro beam at the guided-end where $(x = L)$

$$d = w(L) = \frac{F}{24EI}L^3. \tag{3.13}$$

Thus, the force-displacement relationship between forces applied to the micro plate and its displacement can be written as:

$$\begin{aligned} F &= \frac{24EI}{L^3}d = kd \\ \implies \quad k &= \frac{24EI}{L^3} \end{aligned} \tag{3.14}$$

where k is the lumped stiffness of the micro actuator.

3.2.1 Static Analysis

Static analysis determines the unstable pull-in region. Thus it allows designer to find out reasonable actuation voltage that is safe for the electrostatic actuator to operate without damaging the actuator. In the presence of a voltage drop V between the micro plate and the fixed electrode, the electrostatic force acting on the micro-plate is

$$F_e = \frac{1}{2}\frac{\epsilon_\circ A V^2}{(g_\circ - d)^2} \tag{3.15}$$

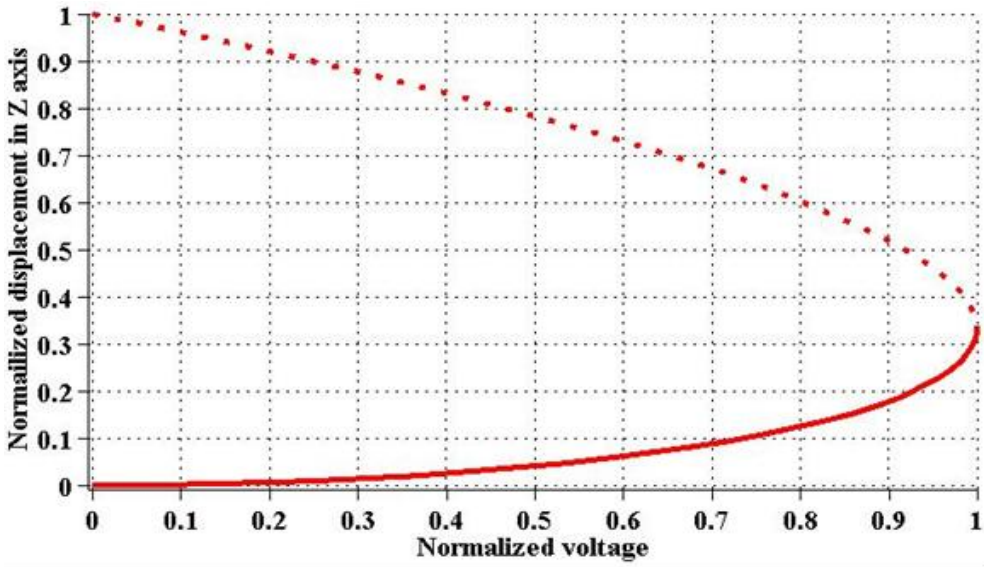

Figure 3.4: Stable and unstable equilibrium positions of the paddle actuator in normalized unitless dimension

This Equation 3.15 is derived from $(Q = VC)$ where Q is charge, V is voltage, and C is capacitance. C for a parallel plate is determined by

$$C = \frac{\epsilon_\circ A}{g_\circ} \tag{3.16}$$

where A is the surface area of the micro-plate, $g_\circ$ is the initial gap between the electrode and micro-plate, and $\epsilon_\circ$ is the permittivity of the air. To evaluate the static equilibrium of the micro plate under this force, we note that at equilibrium the restoring force (kd) and the electrostatic force are equal

$$\frac{24EI}{L^3}d = \frac{1}{2}\frac{\epsilon_\circ A V^2}{(g_\circ - d)^2}. \tag{3.17}$$

Solving Equation 3.17 numerically, we obtain the equilibrium positions (fixed points) of the micro plate for a five voltage value V.

Figure 3.4 shows the relationship between the displacement of the paddle actuator, normalized with respect to the initial capacitor gap $g_\circ$, and the applied voltage, normalized

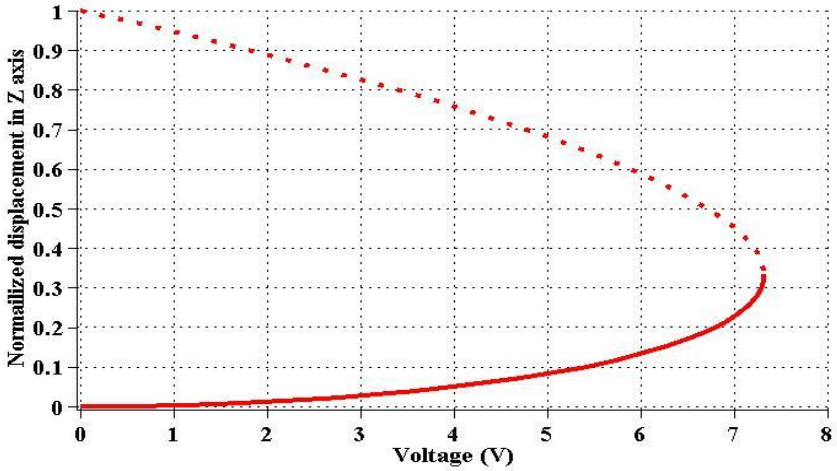

Figure 3.5: Normalized (unitless) displacement Z as a function of applied voltage, V for the paddle actuator

with respect to the pull-in voltage. For each voltage value there are three equilibrium position, a small stable equilibrium, shown as a solid line, a large unstable equilibrium, shown as a dot, and an un-physical equilibrium position larger than the capacitor gap, not shown. Near an unstable equilibrium, a small disturbance causes the micro actuator to move away from the balanced equilibrium, but near to a stable equilibrium and under a similar perturbation the micro actuator comes back to its balanced equilibrium state.

The stable and unstable branches of equilibrium positions meet at the pull-in voltage. The micro actuator snaps down to the fixed electrode for voltages larger then the pull-in voltage. We found the pull-in voltage of the micro actuator corresponds to a displacement equal to one third of the capacitor gap $g_\circ$ as expected for a rigid parallel-plate electrostatic actuator.

The displacement-voltage curve for the micro actuator under study is shown in Figure 3.5. The actuator parameters are listed in Table 3.1. It shows that the pull-in voltage of

the paddle actuator is approximately 7.4 Volts. The displacement is still in the normalized form. For the experimentally measured initial capacitor gap of $g_\circ = 1.75\mu$m, the maximum stable displacement as indicated by the figure corresponds to $0.61\,\mu$m. Unlike applications such as MEMS switches that require actuation over the full-range of the initial gap, avoiding pull-in is essential for the operation of the MEMS demodulator. Further, the RMS voltage applied to the paddle actuator should be limited up to 3 V since the demodulator proper operation is predicated on the availability of an actuator operation range where displacement corresponds linearly to the baseband signal according to the graph in Figure 3.5.

3.2.2 Dynamic Analysis

The equation of motion of each of the micro beams supporting the paddle actuator can be written as [Nayfeh's Nonlinear Interactions]:

$$EI\frac{\partial w^4}{\partial x^4} + m_b\frac{\partial w^2}{\partial t^2} + c\frac{\partial w}{\partial t} = N\frac{\partial w^2}{\partial x^2} + \frac{EI}{2L}\frac{\partial w^2}{\partial x^2}\int_0^L \left(\frac{\partial w}{\partial x}\right)^2 dx + q(x), \tag{3.18}$$

The mass per unit length for the beams m_b is

$$m_b = \rho bh, \tag{3.19}$$

where ρ is the volumetric density of silicon. The damping coefficient is in general made of two components

$$c = c_v + c_s, \tag{3.20}$$

viscous damping c_v and squeeze film damping c_s. In micro structures, squeeze film damping has greater effect on the overall dynamic behavior of the micro system. For simplicity, we use a general viscous damping coefficient c that approximates both effects around a known static equilibrium position.

The first term on the right side of Equation 3.18 represents membrane stiffness the second term represents mid-plane stretching of the beam, and the last term is the transverse distributed load. In static analysis, all time derivative terms on the left hand side of the equation are disregarded; thus, only the first term remains. A simplified form of this general beam Equation 3.18 reduces to the lumped-mass model shown in Equation 3.1.

Similarly, we can reduce Equation 3.18 to the lumped spring-mass-damper model of the paddle micro actuator expressed as follows:

$$m_e\ddot{z} + c\dot{z} + kz = \frac{1}{2}\frac{\epsilon_\circ A V^2}{g_\circ^3(1-z)^2}. \tag{3.21}$$

where z is the nondimensional displacement of the micro plate

$$z = \frac{d}{g_\circ} \tag{3.22}$$

and the overdot denotes a time derivative. The effective mass m_e of the paddle actuator is calculated from:

$$m_e = m_p + 0.75 m_b L, \tag{3.23}$$

where m_p is the micro plate mass and the effective mass of a beam vibrating in the first flexural mode is 0.375 of its total mass. Dividing Equation 3.21 by the effective mass m_e, we obtain the canonical form of the lumped system equation of motion

$$\ddot{z} + 2\zeta\omega\dot{z} + \omega^2 z = f(z), \tag{3.24}$$

where

$$\omega = \sqrt{\frac{k}{m_e}} \tag{3.25}$$

is the natural frequency of the paddle actuator and the damping ratio ζ is related to the damping coefficient c by

$$c = 2\zeta\omega m_e = 2\zeta\sqrt{k m_e} \tag{3.26}$$

In multi-physics analysis, damping is usually expressed in terms of the quality factor Q. It is related to the damping ratio ζ by

$$Q = \frac{1}{2\zeta}. \tag{3.27}$$

The electrostatic force, $f(z)$, acting on the micro plate can be written as

$$\begin{aligned} f(z) &= \frac{1}{2m_e} \frac{\epsilon_\circ A V^2}{g_\circ^3 (1-z)^2} \\ &= \frac{1}{2m_e} C_m \frac{V^2}{g_\circ^2 (1-z)}, \end{aligned} \tag{3.28}$$

where the capacitance across the moving plate, C_m, varies as z varies.

Analyzing the overall dynamic behavior of the MEMS demodulator require coupling the mechanical response of the paddle actuator, analyzed above, to the electrical actuation voltage supplied by the resonant drive circuit. The drive circuit consists of a resistor R, an inductor L, and a capacitor C. Resonance means that the circuit is driven at at its natural frequency

$$\omega_e = \sqrt{\frac{1}{LC}} \tag{3.29}$$

The capacitance of the resonant drive circuit is the sum of the capacitances of the micro plate C_m and the parasitic capacitance C_p of the actuator

$$C = C_m + C_p \tag{3.30}$$

The ratio of C_p to the initial capacitance of the micro plate $C_\circ$

$$r = \frac{C_p}{C_\circ} \tag{3.31}$$

r, which typically ranges from 10 to 1000. The initial capacitance, $C_\circ$, depends on the geometry of the micro plate

$$C_\circ = \frac{\epsilon_\circ A}{g_\circ}, \tag{3.32}$$

where the surface area of the micro plate A is the product of its length L_p and width b_p

$$A = L_p b_p. \tag{3.33}$$

Therefore, the micro plate capacitance C_m is related to its initial capacitance by $C_\circ$

$$C_m = \frac{\epsilon_\circ A}{g_\circ(1-z)} = \frac{C_\circ}{(1-z)}, \tag{3.34}$$

We can also rewrite the electrostatic force as

$$f(z) = \frac{1}{2m_e} C_\circ \left(\frac{V}{g_\circ(1-z)} \right)^2 \tag{3.35}$$

The electrical quality factor Q_f of the resonant drive circuit can be evaluated from the relationship:

$$Q_f = \omega_\circ \frac{Energy\ stored}{Power\ loss} \tag{3.36}$$

The natural frequency of the resonant drive circuit when the actuator is at rest $\omega_\circ$ can be found experimentally. It is related to the capacitance ratio r by:

$$\omega_\circ = \sqrt{\frac{1}{L\ C_\circ\ (r+1)}} \tag{3.37}$$

Once the quality factor of the resonant drive circuit Q_f is measured experimentally, the parasitic resistance in the circuit R can be found from the relationship:

$$Q_f = \sqrt{\frac{1}{R^2\ C_\circ\ (r+1)}} \tag{3.38}$$

Figure 3.6 shows a Simulink model corresponding to Equation 3.21, the equation of motion for the paddle actuator. Table 3.1 lists the dimensions and material properties of the paddle structure used to obtain the numerical results of lumped-mass and the Simulink models. The numerical values are actual dimensions of a micro-plate under the test as per design specification for fabrication developed for mass sensor [31]. However, the initial gap, $g_\circ$, is obtained by experiment.

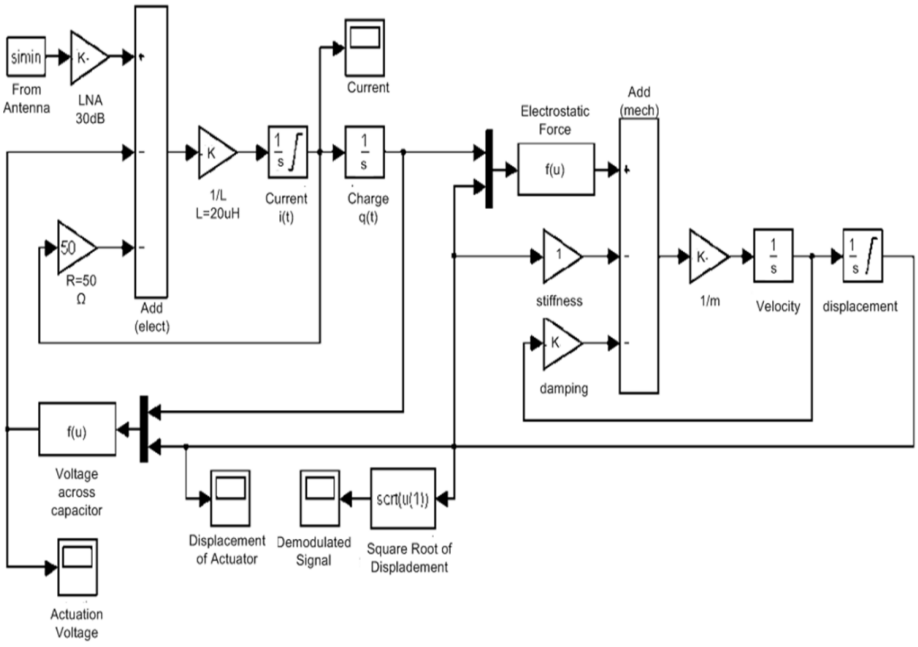

Figure 3.6: Simulink model used to numerically simulate the paddle actuator

The electrostatic force, denoted by $f(u)$ in the Simulink mode, is calculated from:

$$f(u) = \frac{1}{2} C_\circ \left(\frac{V}{g_\circ (1 - z)} \right)^2, \tag{3.39}$$

where the input voltage across the capacitor, V, to the actuator depends on the charge, q, and displacement, z. Detailed derivation of the equation is omitted in this section, but essentially, the Equation 3.40 is elaborated form of $V = Q/C$. The final equation placed in the function box for voltage across the parallel plate in simulation is expressed as:

$$V(q, z) = \frac{q(1 - z)}{C_\circ (r(r - x) + 1)}, \tag{3.40}$$

In simulations, we set the damping of the actuator to critical damping $\zeta = 1$ to minimize the actuator settling time. We also set the damping ratio to values similar to those of practical actuators, $\zeta = 0.01$ and $\zeta = 0.001$, in order to observe the effect of damping on the quality of the output baseband signal.

Several paddle actuators with various features in their design, we switched namely initial capacitor gap, support beam length, and paddle area. It is worth noting that the natural frequency of the actuator depends on its effective mass and stiffness. The dominant parameter controlling the stiffness of the paddle actuator is the beam length L because it appears as L^3 in the denominator of the stiffness, Equation 3.14. Although the beam thickness h also appears as h^3 in the numerator of the stiffness equation, realistically the beam thickness can not be changed. The standard MEMS fabrication process used to produce the actuator, polyMUMPs [33], limits the deposition thickness of the structural polysilicon layer to either $2\,\mu$m or $1.5\,\mu$m. In this case, structural polysilicon layer Poly1 was used to fabricate the actuators and their thickness was set to $h = 1.5\,\mu m$.

Up to this point, our analysis adopted the design parameters of the paddle actuator. The design value of the initial gap is $g_\circ = 1.75\,\mu$m, however experimental measurements on paddle actuator prototype shown in Figure 3.7. The initial gap, $g_\circ$ is $1.14\,\mu$m. Thus

Table 3.1: Dimensions and properties of the fabricated paddle actuator

Symbol	Definition	Value for Paddle Actuator # 12
E	Young's Modulus	160 GPa
$\epsilon_\circ$	Permittivity	8.854×10^{-12} F/m
ρ	Density	2330 kg/m^3
$g_\circ$	Initial gap $**$	1.14 μm
L	Beam length	100 μm
b	Beam thickness/width	10 μm
h	Beam height	1.5 μm
m_b	Beam mass	6.99×10^{-12}
L_p	Plate length	100 μm
b_p	Plate thickness/width)	100 μm
h_p	Plate height	1.5 μm
m_p	Plate mass	3.495×10^{-11}
m_e	Total effective mass	3.757×10^{-11}
K	Stiffness	10.8 N/m
A	Area of parallel plate	1×10^{-8} m^2
c	Damping coefficient	4.028×10^{-5}

Table 3.2: Electrical parameters for micro-fabricated paddle structure

Symbols	Definitions	Values for Paddle Actuator # 12
V_{pi}	Pull-in voltage	7.3 V
R	Resistance	50 Ω
L	Inductance	6.8 mH
$C_\circ$	Initial capacitance	77.7 fF
C_p	Parasitic capacitance	7.77 pF
r	$C_p/C_\circ$ $**$	100
C_{cap}	Total capacitance	7.85 pF

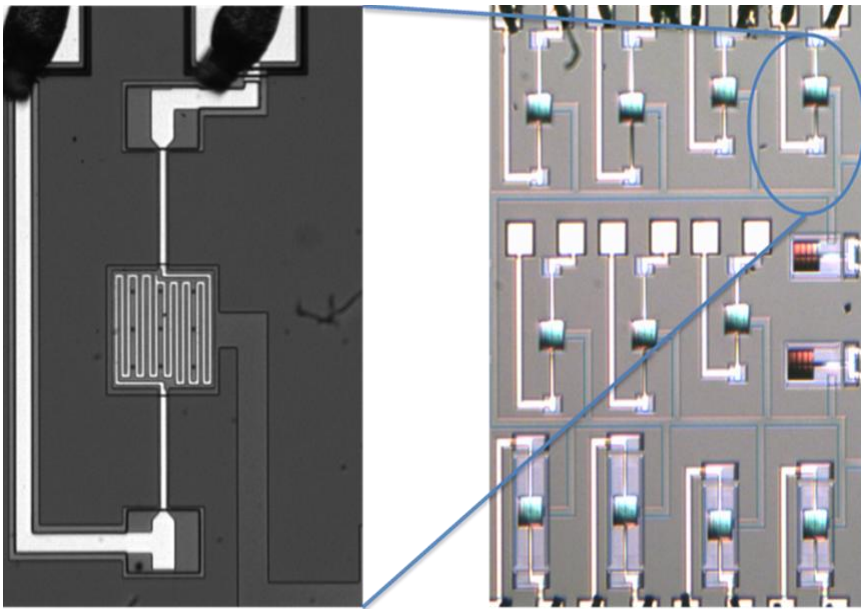

Figure 3.7: Wire-bonded paddle actuator

Table 3.3: Beam characteristics summary

Paddle Actuator Type	A	B	C	D
Beam Length (μm)	100	100	150	150
Natural Frequency (kHz)	102.038	102.038	54.8624	54.8624
Stiffness $k(N)$	15.12	15.12	4.48	4.48
Effective Mass M_e (g)	3.68×10^{-11}	3.68×10^{-11}	3.77×10^{-11}	3.77×10^{-11}
Initial gap $g_\circ$ (μm)	0.75	2.75	0.75	2.75
Pull-in Voltage V_{pi} (Volts)	4.7	32.5	2.6	17.7

for the following simulations, this gap value will be adopted in order to closely predict the real actuator response. Figure 3.7 shows enlarged picture of the paddle actuator used for experiment on the left and the rest of the paddle actuators with various beam lengths on the right. Finding the actual values of the initial gap for these actuators involved a process of parametrization: an iterative process where experimental measurements were plugged into the model presented above and compared to other experimental measurements until they were matched. Parameters marked by two asterisks $**$ in Table 3.2 indicate values are measured experimentally via a process of parametrization.

Four different types of the double beam paddle actuators similar to the ones in right side of Figure 3.7 were available for demodulation experiments. They have identical dimensions except for the support beam length and initial gap. The paddle actuators beam length, effective stiffness, effective mass, initial capacitor gap, and pull-in voltage are listed in table 3.3. Double beam paddle actuator in Table 3.3 were to give a clear idead about the corelation between the pull-in voltage and initial gap as well as the beam length. Large initial gap requires higher voltage for actuation. The longer the beam length, the less voltage is required for pull-in to occur. Based on the prefabricated dimensions, type D is

the most ideal case for demodulator experiment. The electrostatic actuator is operated in the range of voltage that is less than half of the pull-in voltage to stay in the linear-like region.

3.3 Micro-Actuator Type II: Plate Actuator

This section will not show all the details of static and dynamic analysis. It will briefly cover modeling electrostatic actuator type II, a plate at the end of a cantilever beam actuator. Recent work of Towfighian [34] on a large-stroke electrostatic micro-actuator describes the cantilever beam model development using Galerkin's method. Since the full dynamic stroke range of operation is not required for the purpose of MEMS demodulation, snap shot of numerical sets of values for all the parameters required for a specific actuation voltage is used. A closed-form expression for the static detection developed by Khater *et al.* [35] as the following:

$$M_{11}\ddot{z}_1 + D_{11}\dot{z}_1 + K_{11}z_1 = J_1 + R_1(V_{DC} + V_{AC}(t))^2 H(z_1). \tag{3.41}$$

Coefficients for Mass is demoted as M, damping D, stiffness K, and subscription $_{11}$ denotes first mode. J_1 is a constant numerated based on static displacement of a specific point along the length the beam, R_1 is a coefficient attached to time-varying input voltage, and H is function of z_1 which is displacement toward bottom electrode. The purpose of quoting Equation 3.41 is because this lumped model takes similar pattern as Equation 3.21. This enables the numerical calculations for static analysis which determines characteristic of the pull-in phenomenon. Choosing one operational voltage and determining the coefficient corresponding to the specific voltage simplifies the computation of the numerical simulation model. The same numerical parallel plate model can be reused for micro-actuator type II by plugging in the values for the coefficients.

3.4 Numerical Simulations

In this section numerical simulations for type I actuators are carried out for analog demodulations and digital demodulations.

3.4.1 Simulation of AM Demodulation

The period, T, at the electrical resonance is 1/219 kHz, which is 4.566 μs. For a smooth curve, 20 points per period is required. Thus, the step size is set to 0.23 μs. Figure 3.8 is a screen capture of simulations. The baseband signal consists of two sinusoidal signals:

$$\begin{aligned} S_1 &= 1.0\ \sin(2\pi 1000t) + 1.1 \\ S_2 &= 0.5\ \sin(2\pi 500t) + 0.51. \end{aligned} \tag{3.42}$$

All the values are arbitrarily chosen for the demonstration purpose. However, the amplitude and frequency are varied to show two tones. The DC values are added to prevent zero crossing by adding extra off-set. ODE3 Bogacki-Shampine is used to compute the integrations.[36] There are many ways of choosing a solver. A proper solver helps meeting target accuracy. A fixed-step solvers step size remains constant, and a variable-step solvers step size varies depending on the dynamics of the system: rapid changes require smaller steps to achieve accuracy while slow changes require smaller steps to model the system. In our case, a fixed-step is used to explore the dynamics of the system. The baseband signal is mixed with a high frequency carrier signal. Since the final application is for demodulation, a fixed-step solver is chosen to carry out a real-time computation. Discussing how the Bogacki-Shampine method works is not part of this report. There are five ordinary differential equation (ODE) solvers in Simulink numerical solver: ODE1 is the least complex integration method and ODE5 is the most complex integration method. ODE3 is recommended as a starting point for solving the model for accuracy and reasonable computation

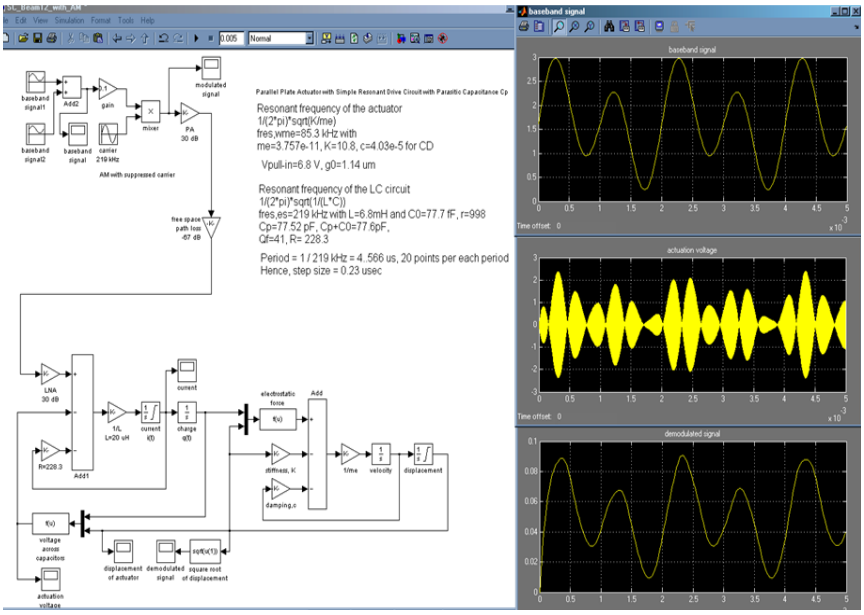

Figure 3.8: AM demodulations simulations for resonance carrier frequency at 219 kHz

demand. Figure 3.9 captures three system responses to the three different damping coefficients: heavily over-damped, OD (ζ=100); over-damped (ζ=10); and critically-damped, CD, (ζ=1). The paddle structure responds to the electrostatic actuation enabled by RLC resonance circuit in bottom left side of Figure 3.8. Starting at the critically damped case a small distortion appears at each maximum peaks. When the mechanical damping factor is decreased to below 1, whether ζ is 0.1 or 0.01, the same distorted-top characteristics were observed. Figure 3.10 shows a displacement curve at three damping coefficients with a carrier frequency of 219 kHz. The lower damping coefficient (i.e ζ is less than 0.5) at this frequency displays the same response as the under-damped case where ζ is 0.5. Figure 3.11 is simulated with exactly the same parameters except that the inductance value has been changed to 680 μH from the previous simulations. The following is the damping response of the MEMS demodulator displacement with a carrier frequency of 693 kHz at Q=50 and Q=500. Often a RF MEMS such as a resonator desires a high Q value since the selectivity and accuracy of response to a specific frequency is necessary. However, our MEMS demod-

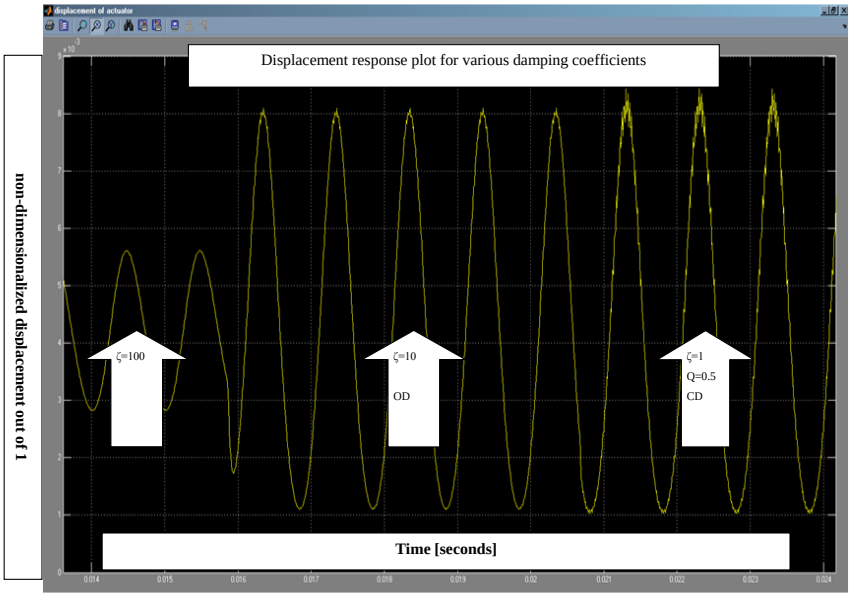

Figure 3.9: Displacement graph for over damped and critically damped cases

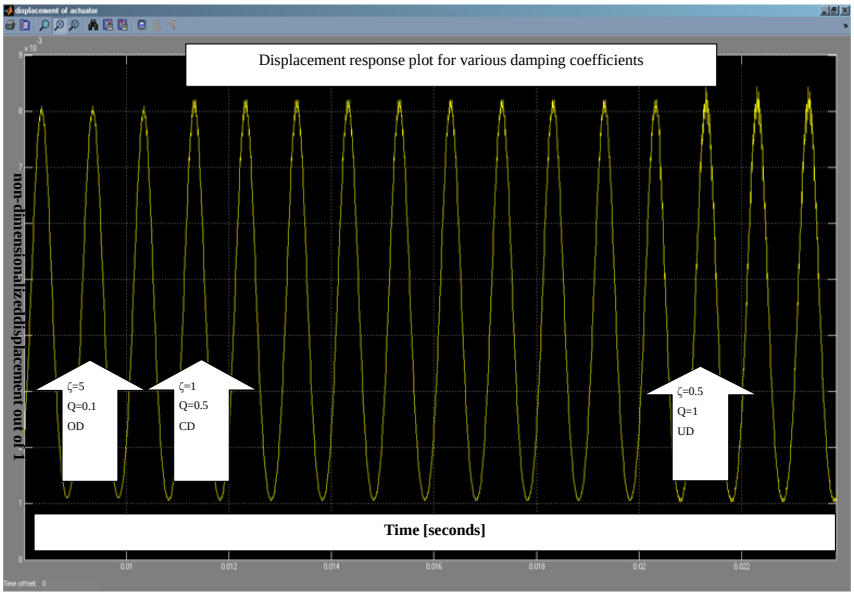

Figure 3.10: Displacement comparison graph for critically damped and under damped cases

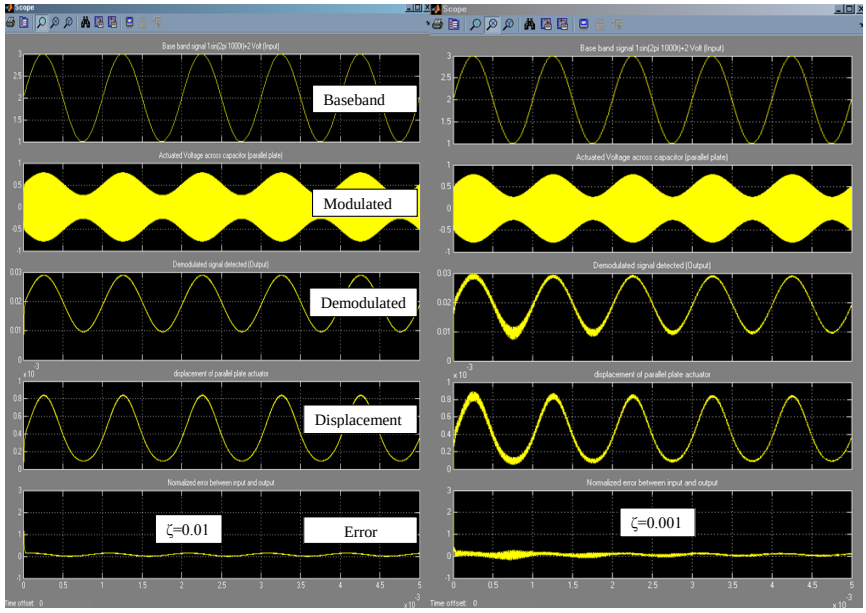

Figure 3.11: Displacement graph to damping coefficient ζ=0.01 and ζ=0.001 at 693 kHz

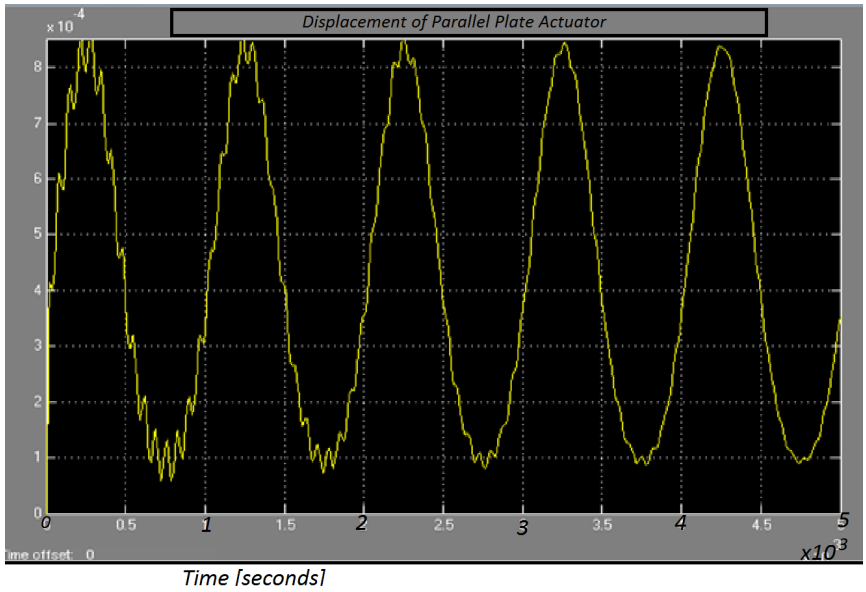

Figure 3.12: Displacement response to damping coefficient ζ=0.001 (Q=500) at 693 kHz

ulator works better with low Q values (0.5 10). When the frequency response less sharp at the resonance, there are more room (thus more operable bandwidth) is available for the demodulation. A reasonable mechanical stiffness will provide a cleaner signal than will a severely under damped micro-plate that would be too sensitive to external forces. Since the nature of the baseband signal ranges anywhere between 20 Hz to 20 kHz, the mechanical resonance of the electrostatic actuator must be higher than 20 kHz as one of design criteria. Also, a minimum input signal level is required to drive the RLC resonance circuit. Although supplying half of the pull-in voltage is a good place to start, a precise value of minimum input has not yet been determined since the simulation model is an ideal case. Figure 3.11 shows two under-damped systems. When the damping coefficient is reduced to one thousandth, it takes extra periods to reach a clean demodulated signal, as shown in Figure 3.12. The results FM demodulation simulations and experimental demonstration are shown in Section 3.4.2.

3.4.2 Simulation of FM Demodulation

The same device is used for FM demodulation. Since exactly the same micro paddle structure will be used to conduct FM demodulations, similar results are expected. Current simulations using the same value of inductor gives a carrier frequency that is too close to the electrical resonance. Thus, an inductor with a smaller value will be used in the future for both simulations and experiments. The input signal is sine wave 1.8 volts peak-to-peak. The actuation voltage ranges between -2 volts to + 2 volts. The displacement ranges between 6.5 $\times 10^{-5}$m to 7.25$\times 10^{-5}$m. The demodulated signal ranges from 0.05 mV to 0.55 mV. Further analysis and optimization will be useful to find out characteristics of FM demodulations. This simulation result is to show that it is possible to conduct FM demodulations using exactly the same paddle structure as an FM demodulators. A desired carrier frequency can be chosen by selecting an appropriate external inductor. The higher

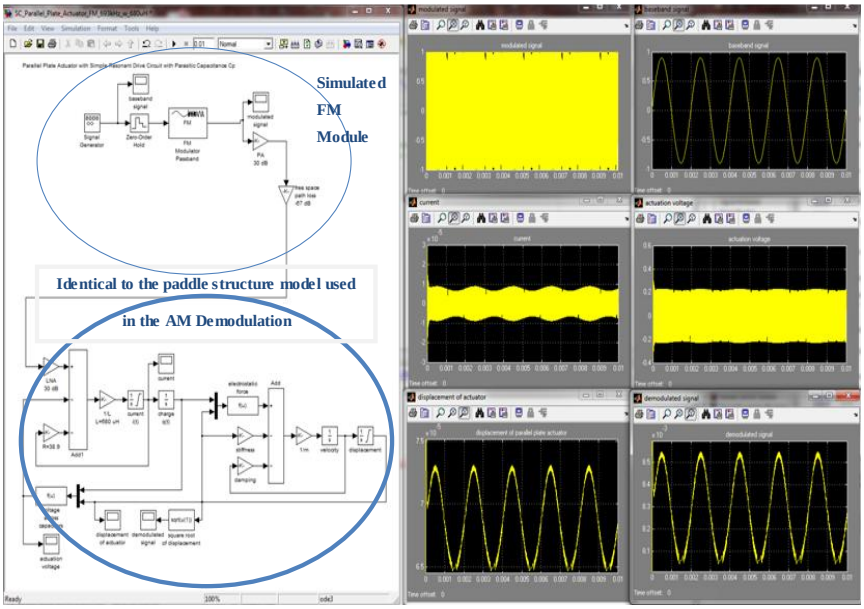

Figure 3.13: FM Demodulations Simulations

the value of off-the-shelf inductor is, the lower the natural frequency of the resonance circuit will be.

3.4.3 Simulation of Digital Demodulation

Numerical simulation for ASK and FSK demodulation is presented in the following. First, a random on-off, ones and zeros, digital signal is generated. For ASK modulation scheme, one is multiplied at electrical resonance, and so are zeros. The modulated signal show filled-box-like shape for signal represented by $\pm$ 1 Volts, and a flat-line for zero. Current applied to the resonance circuit that includes the parallel plate follows the shape of modulated signal input. The amplified voltage at approximately $\pm$ 10 Volts actuates the parallel micro-plate. In numerical simulation the demodulated signal is a square root of the calculated displacement, x. Details are already shown in Figure 3.6 which is same as what is on the left side of Figure 3.14. The paddle type parallel micro-plate ASK Simulations result in

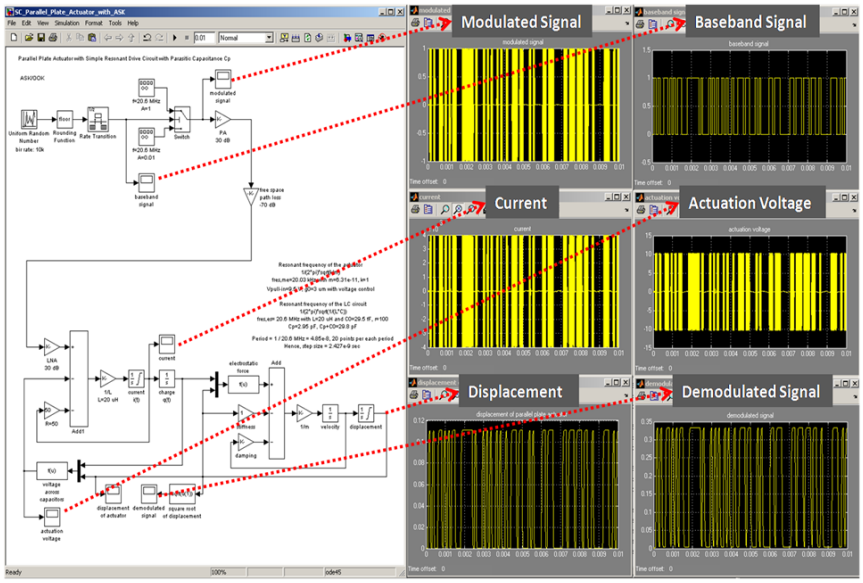

Figure 3.14: ASK Demodulations Simulations

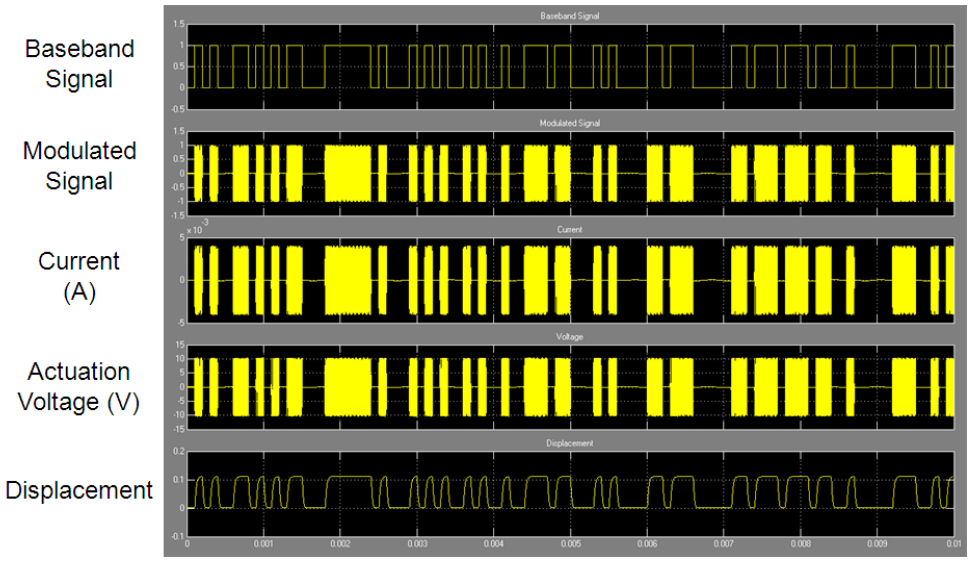

Figure 3.15: Paddle Type Parallel Micro-Plate ASK Simulations Results Zoomed Up view.

the right side of Figure 3.14 have corresponding dotted lines across the figure indicating the location of corresponding probing points to the simulations result on the left. The zoomed up version of the same ASK simulations results is recaptured in Figure 3.15. FSK

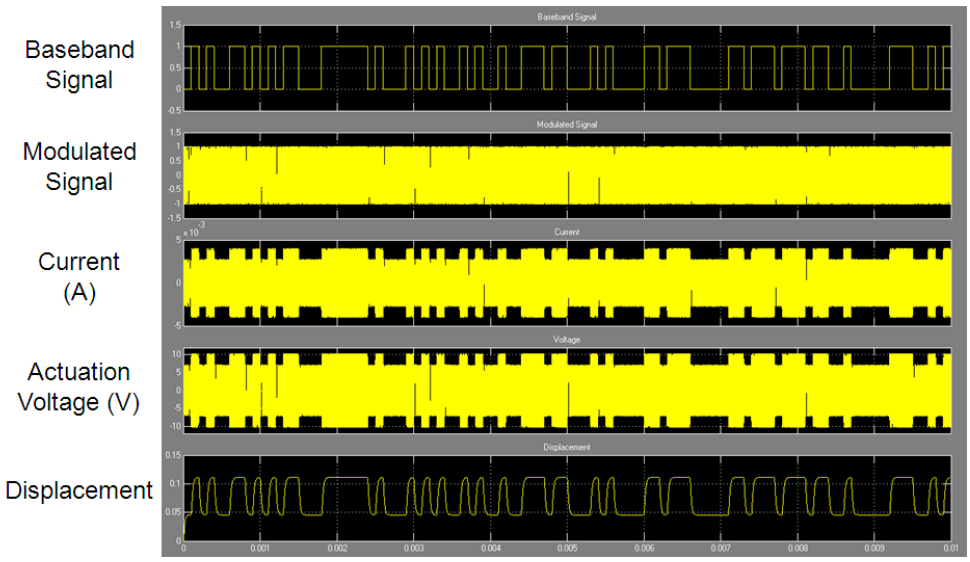

Figure 3.16: Paddle Type Parallel Micro-Plate FSK Simulations Results Zoomed Up view.

modulation scheme is used in place of the input signal in Figure 3.16 that shows zoomed up version similar to the ASK simulations results. What is worth noting is the modulated signal now shows similar filled-box-like shape for signal represented by $\pm$ 1 Volts, and a flatter-box-like shape with drastically reduced amplitude due to off-resonance for zero.

Chapter 4

Experimental Verification

This chapter contains AM/FM ASK/FSK demodulation hardware experiment results and numerical experiment results for both type I paddle actuator and type II plate actuator.

4.1 Experiment Setup

A resonant drive circuit in [37] and a phase detector circuit were designed, built, and provided for these MEMS demodulation experiment. The testing results validate the circuits for the future experimental opportunities and applications for other purposes which are not scope of this thesis. However, for clarity and understanding, the architecture and functionalities of the circuits are explained in the following sections.

4.1.1 Resonant Drive Circuit

Both the two types of electrostatic actuators' varying capacitance is an essential part of the resonant drive circuit. Figure 4.1 represents a MEMS Demodulator resonant driving circuit. A signal with high impedance coming in to the input terminal is buffered by an

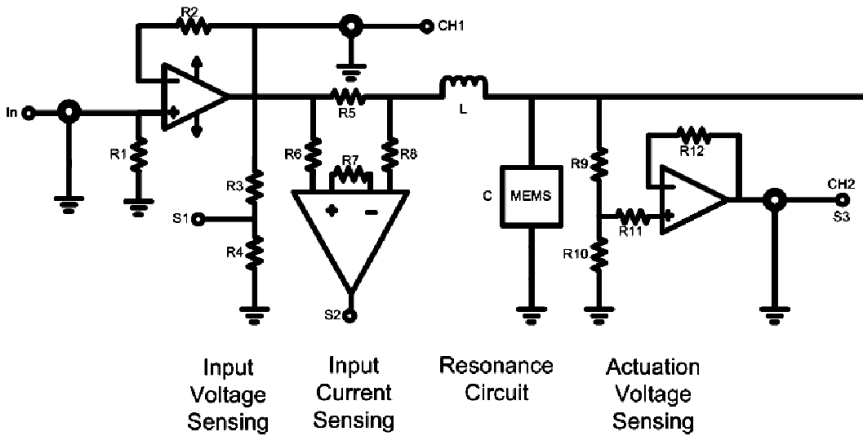

Figure 4.1: MEMS demodulator actuation driving circuit

operational amplifier (OpAmp) (LM78L05) in the first stage. This OpAmp works as a voltage follower, where the $R1$ and $R2$ have the same value. The output of the buffer is measured at a test point labeled CH1. R3 and R4 are resistors for a voltage divider that allows measurement of the applied voltage at a comparison point labeled S1, also known as an input voltage. R6 and R8 are balance-input resistors for the input of an instrumentation amplifier for current sensing (1NA217). This senses a current passing through R5, which is in range of hundreds ohms, gives a tiny voltage drop. R7 dictates the gain measured at the comparison point labeled S2. The output of this OpAmp is connected to the LC resonance circuit. The capacitance is created by the MEMS parallel plate, the paddle structure, in our case. Resistors R9 and R10 are voltage divider that goes through buffer which prevents high through rate oscillation that may occur due to the current input to the negative channel of the OpAmp (LM78L05). The actuation voltage is measured at a test point labeled CH2, which is also a measurement point labeled S3.

An initial capacitance of a micro-plate with an air gap ranging from 0.75 μm to 2.75 μm is less than 100 ${}_fF$, and the ratio between the parasitic capacitance ranges from 10 to 100. Thus, for choosing the resonance frequency, $f_\circ$, which is a carrier frequency in

Table 4.1: Carrier frequency at resonance and choices of inductors based on the total capacitance value

L	C_{tot}	f_o
22 mH	1 pF	1.07 MHz
10 mH	2 pF	1.125 MHz
100 nH	1 pF	503 MHz
10 nH	1 pF	1.590 GHz

this MEMS demodulator case, the value of the inductance, L, is chosen among available standard components and based on the expected total capacitance, C_{tot}, as shown in Table 4.1.

4.1.2 Phase Difference Detection Circuit

Phase difference detection circuit is explained in this section. There are numerous off-the-shelf phase detectors in the market. However, for the specific need of comparing the modulated input voltage and modulated actuation voltage by counting the zero-crossing of each test point and comparing with a phase comparator, phase detection architecture is envisioned as shown in Figure 4.2. This phase comparator circuit was originally developed for full-range displacement sensing for chaotic controller by Park in [3]. In order to realize a fully functioning, portable, stand-alone, MEMS demodulation device, this part of circuit is added to the MEMS demodulator circuit instead of relying on the optical sensing using external device such as a vibrometer. The block diagram in Figure 4.2 shows how phase difference between the modulated actuation voltage and the modulated input voltage is measured. Detailed circuit schematics of a zero-crossing detector is shown in Figure 4.3. A zero-crossing detector is employed to detect the FM modulation. A high speed com-

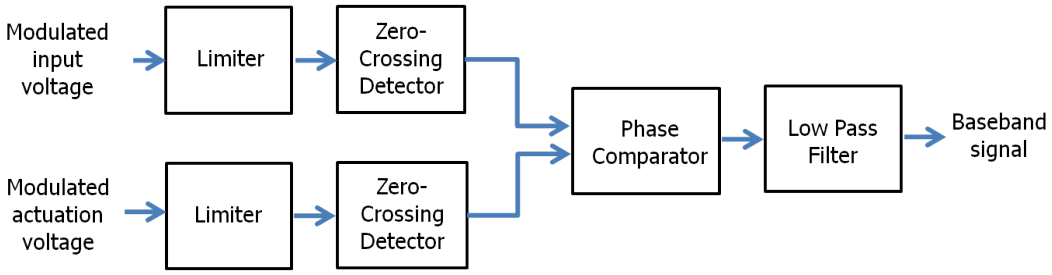

Figure 4.2: Block diagram of Phase Detector that measures the phase difference between input voltage and actuation voltage

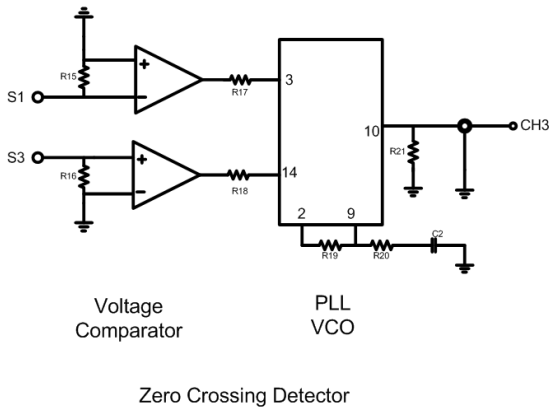

Figure 4.3: Zero crossing voltage phase comparator

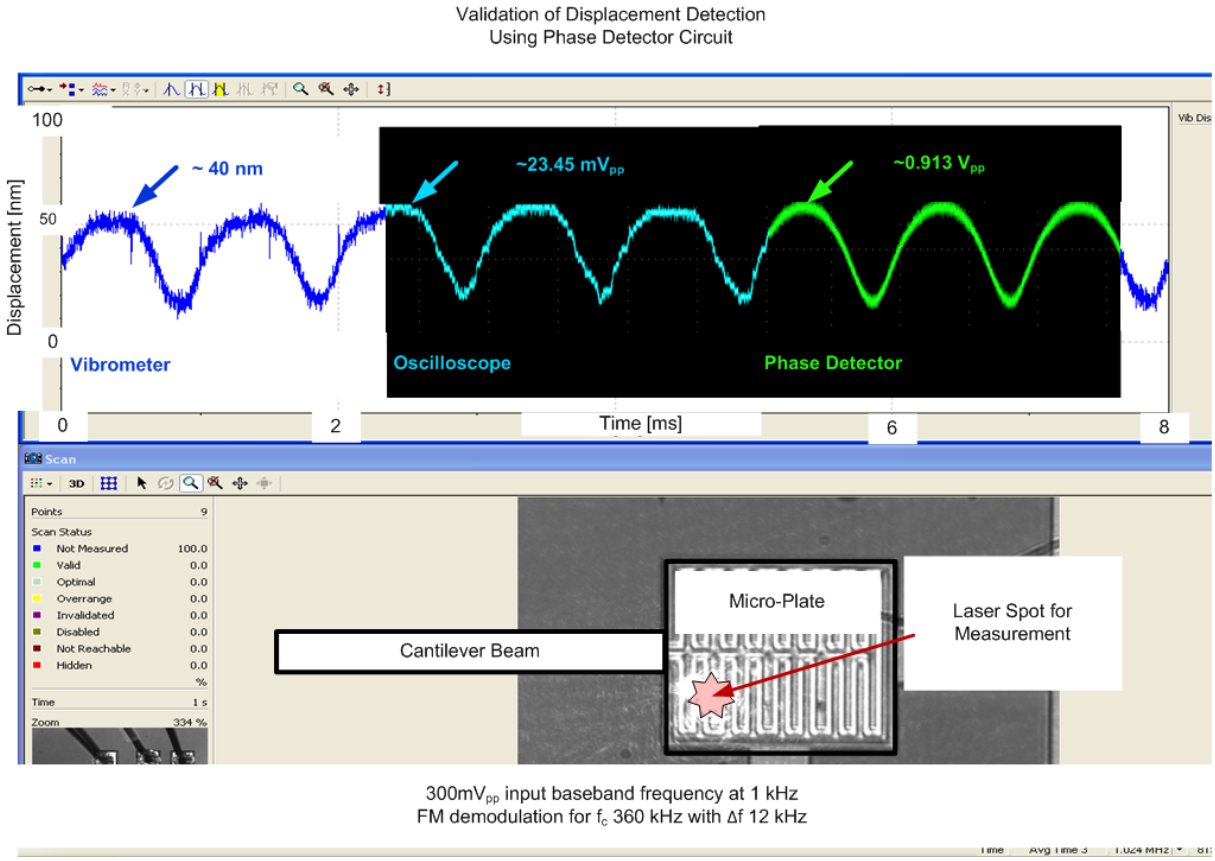

Figure 4.4: Validation of Displacement Comparing Vibrometer Displacement Decoder Measurement to Detection Using Phase Detector Captured in Oscilloscope

parator (MAX907) and a phase locked loop(PLL) with a voltage control oscillator (VCO) (HC4046A) in Figure 4.3 compares signal from the input voltage from measurement point S1, and the actuation voltage from the measurement point S3. The phase difference of current is also measured at the test point labeled CH3. Phase changes in current is also measured in a similar manner.

4.2 Validation of the Displacement Sensor

Figure 4.4 is superimposed screen captures of displacement measurement for MEMS demodulation with a baseband frequency of 1 kHz with 300 mV peak-to-peak input voltage for 360 kHz FM carrier frequency with a 12 kHz frequency deviation provided by a function generator. An oscilloscope screen capture in dark background is superimposed on the vibrometer's screen capture. The top left and top centre are signals from the output channel on the OFV 5000 Polytec vibrometer controller's displacement decoder. Top right wave is an oscilloscope screen capture of a signal from a phase detector circuit. As clearly shown in Figure 4.4, the superimposed displacement measurement is coherent. For example, 23.45 mV_{pp} on the oscilloscope is 40 nm since these signals are split from the same output. $0.913V_{pp}$ from the phase detector circuit probing point measured on the oscilloscope corresponds to the 40 nm displacement. Thus all the demodulation test results, displacement detection is conducted with the phase detector circuit as part of a fully functioning overall MEMS demodulator device. The presentation mode of the vibrometer allows users to conduct post-experiment analysis, as shown in Figure 4.6. The top frame in the figure shows a picture of the micro-actuator just before pull-in at the location marked by a red vertical line on the centre of the bottom frame. We note that, in agreement with our assumptions, the suspension beams deform while the center micro-plate remains rigid. The bottom frame shows the displacement time-history of a point on the micro-plate as the actuator is excited by a signal.

4.3 Analog Demodulation Hardware Experiment

Both AM and FM demodulation were tested with electrostatic MEMS demodulator. The first sets of AM demodulation test were conducted to find out the minimum detectable signal strength; to compare the output signal strength at electrical resonance with the one

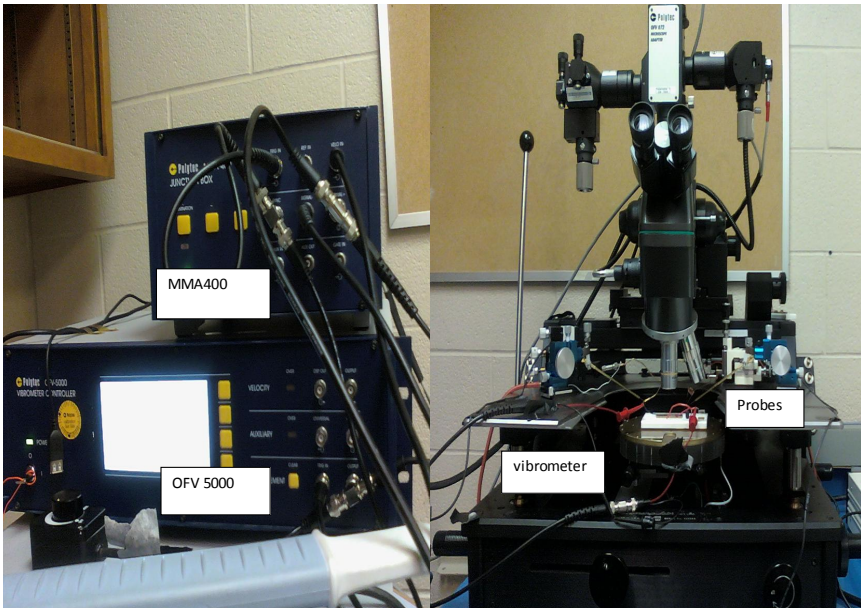

Figure 4.5: Vibrometer MEMS demodulation experiment setup photo

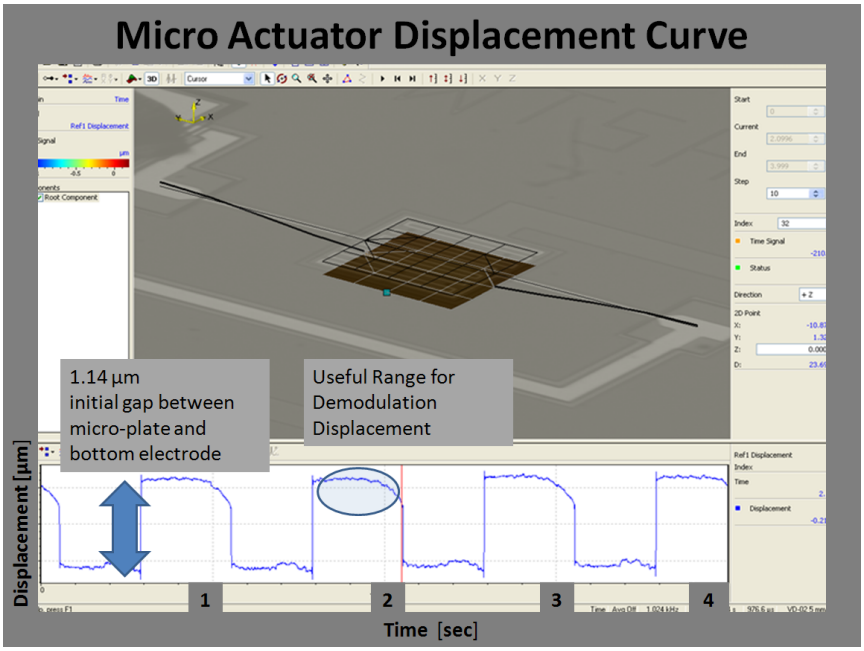

Figure 4.6: A paddle actuator transitioning to pull-in

Table 4.2: Vibrometer MEMS demodulation experiment data summary

Figure Number	Modulated AM Signal	Applied Frequency	Voltage Applied Across Actuator	Displacement for Demodulation	Baseband Frequency
Fig 4.7	159mV	143kHz	6.28V	32.1mV	112Hz
Fig 4.8	211mV	126kHz	2.85V	20.8mV	$NotMeasurable$
Fig 4.9	161mV	138kHz	6.29V	35mV	206Hz
Fig 4.10	161.5mV	137kHz	6.29V	31mV	103Hz
Fig 4.11	160.5mV	137kHz	6.20V	29.7mV	195Hz
Fig 4.12	218mV	122kHz	8.36V	56.9mV	55Hz

which is slightly off the resonance and to detect different baseband frequency.

4.3.1 AM Demodulation

Table 4.2 summarizes Figures from 4.7 to 4.12. Experiments were conducted on the micro-actuator. The natural frequency of the actuator was calculated from the data in Table 3.1 as $f_m = 88.47$kHz. The natural frequency of the resonant drive circuit was set to $f_e = 138$kHz. The micro-plate displacement, representing square of the baseband signal, was captured and recorded using the Polytech^{TM} scanning vibrometer setup shown in Figure 4.5. The results of AM demodulation tests are shown as screen shots of digital oscilloscope in Figures 4.7 to 4.12. In each figure, the AM signal is shown in the top frame in yellow, the actuation voltage applied to the MEMS demodulator is shown in the middle frame in green, and the demodulated signal, the displacement of the micro-plate, is shown in the bottom frame in blue which is set at 2μm/V.

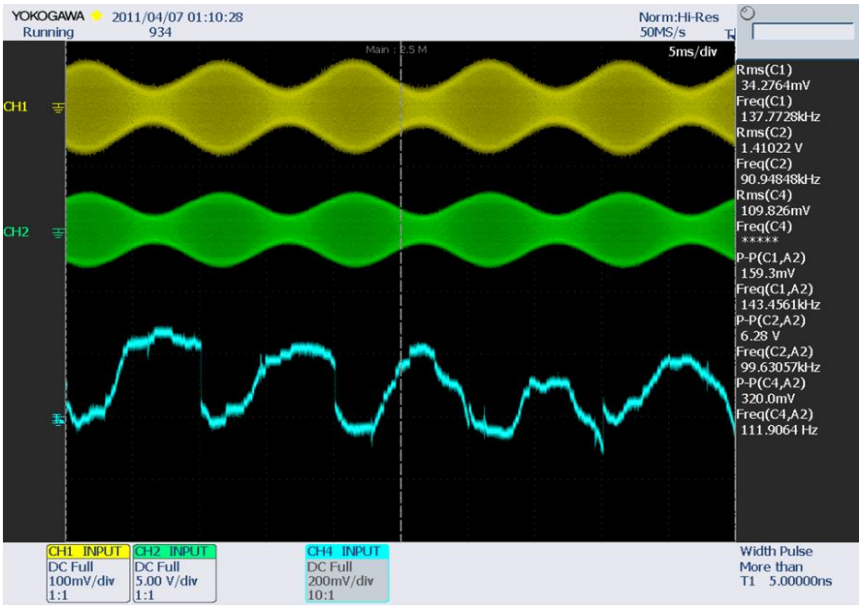

Figure 4.7: Oscilloscope screen capture for s_1

$$s_1(t) = a_1 \cos(2\pi f_1) \tag{4.1}$$

where $a_1 = 48.5$mV and $f_1 = 111.9$Hz mixed with an AM carrier frequency of $f_c = 137.7$kHz. The RMS of the AM modulated signal is 47.3 mV. The RMS of the actuation signal is 1410 mV. The frequency is set not at resonance on purpose. The displacement 109.1 mV RMS is translated to measured displacement of 307 nm which is way above noise level providing a significantly distinguishable baseband signal as expected at the resonance.

$$s_2(t) = a_2 \cos(2\pi f_2) \tag{4.2}$$

where $a_2 = 67$mV and $f_2 = 200$Hz mixed with an AM carrier frequency of $f_c = 127$kHz. The RMS of the AM modulated signal is 47.3 mV. The RMS of the actuation signal is 559mV achieving only 21dB gain. All conditions are same as the Figure 4.11 except the carrier frequency is set not at resonance on purpose. The displacement 4.3 mV RMS is translated to measured displacement of 12.1 nm which is close to noise level providing no

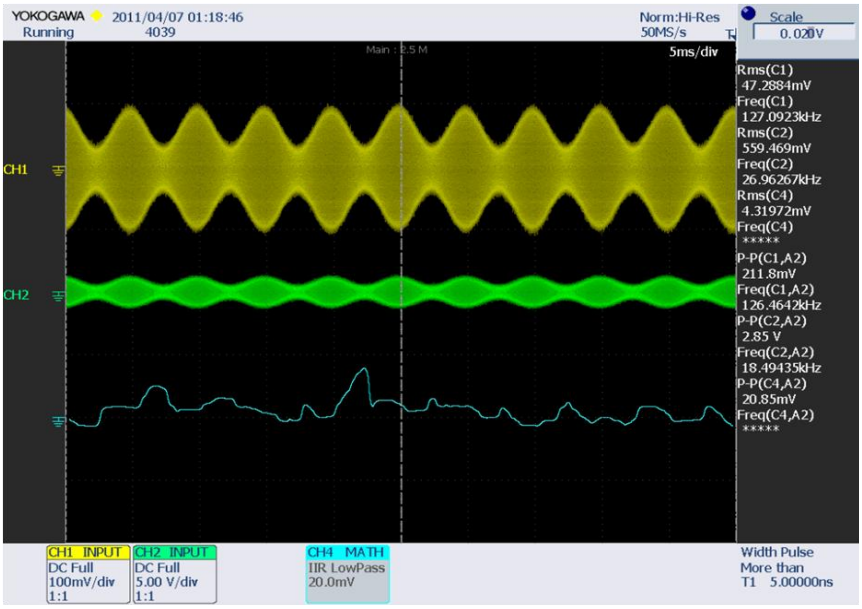

Figure 4.8: Oscilloscope screen capture for s_2

significantly distinguishable baseband signal as expected at the off resonance.

$$s_3(t) = a_3 \cos(2\pi f_3) \tag{4.3}$$

where $a_3 = 48.6$mV and $f_3 = 206$Hz mixed with an AM carrier frequency of $f_c = 138$kHz. The RMS of the AM modulated signal is 34.4 mV. The RMS of the actuation signal is 1.4V achieving 32dB gain. 10.9 mV RMS is translated to measured displacement of 30.8 nm.

$$s_4(t) = a_4 \cos(2\pi f_4) \tag{4.4}$$

where $a_4 = 48.6$mV and $f_4 = 103.5$Hz mixed with an AM carrier frequency of $f_c = 126$kHz. The RMS of the AM modulated signal is 31.6 mV. The RMS of the actuation signal is 1.4V achieving 32dB gain and 10.1 mV RMS is translated to measured displacement of 28.6 nm.

$$s_5(t) = a_5 \cos(2\pi f_5) \tag{4.5}$$

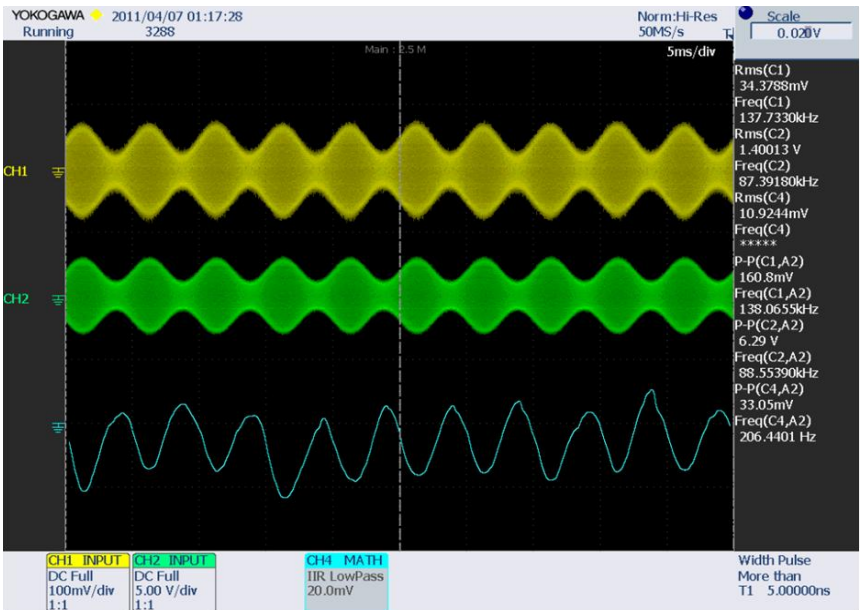

Figure 4.9: Oscilloscope screen capture for s_3

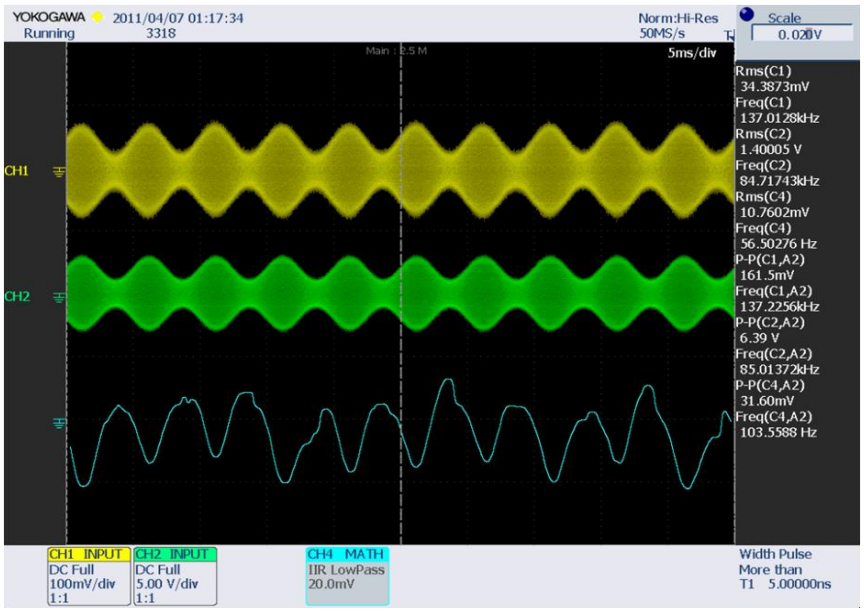

Figure 4.10: Oscilloscope screen capture for s_4

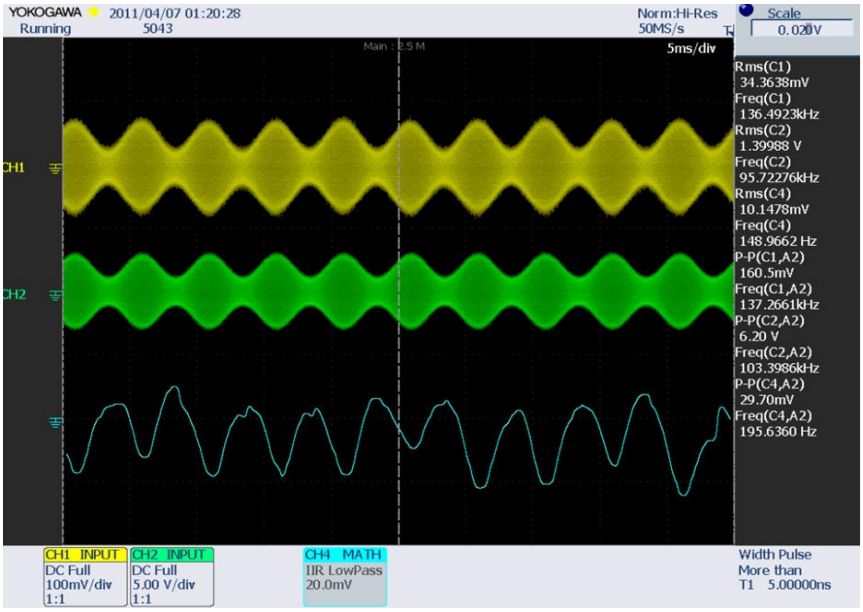

Figure 4.11: Oscilloscope screen capture for s_5

where $a_5 = 48.6$mV and $f_5 = 196$Hz mixed with an AM carrier frequency of $f_c = 137$kHz. The RMS of the AM modulated signal is 34.4 mV. The RMS of the actuation signal is 1.4V achieving 32dB gain and 10.1 mV RMS is translated to measured displacement of 28.6 nm.

$$s_6(t) = a_6 \cos(2\pi f_6) \tag{4.6}$$

where $a_6 = 68$mV and $f_6 = 55.6$Hz mixed with an AM carrier frequency of $f_c = 122$kHz. The RMS of the AM modulated signal is 48.1 mV. Since the carrier frequency in this case approaches the resonant drive circuit natural frequency $f_c \rightarrow f_e$, the 1.92V actuation signal achieves 32 dB gain. 18.7 mV RMS is translated to measured displacement of 52.9 nm. In both cases, the baseband signal is successfully recovered using the MEMS demodulator. A series of Figures in section 4.3.1 shows screen captures of an oscilloscope for AM demodulations in action: different magnitudes of input voltages; different carrier frequencies (one that is not at resonance); and different baseband frequencies. The yellow channel 1 line is the modulated signal going into the resonance circuit, the green channel

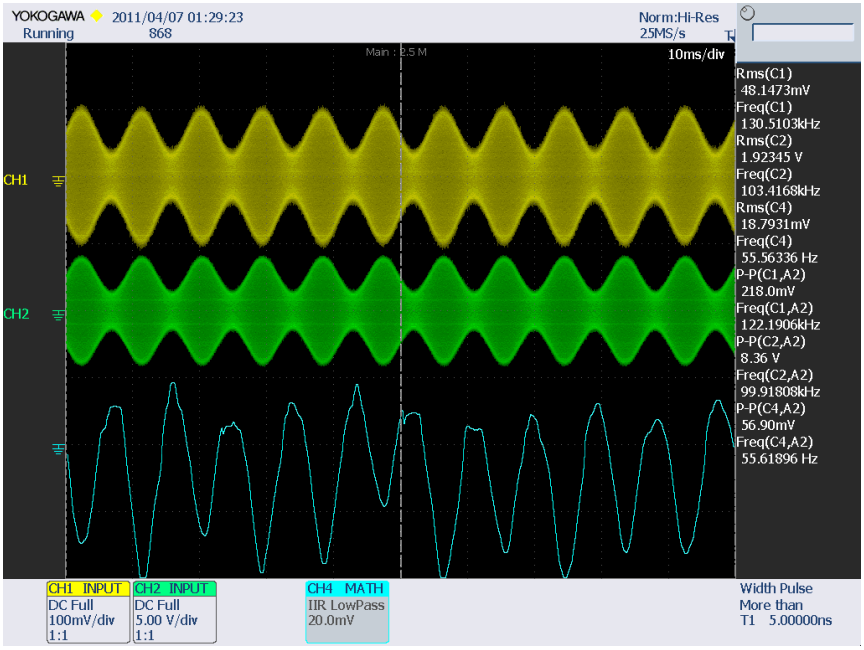

Figure 4.12: Oscilloscope screen capture for s_6

2 line is the actuation voltage seen by the micro-plate capacitor, and the blue channel 4 line is displacement of the micro-plate detected by the vibrometer's displacement sensor. For the preliminary AM demodulation test, we know that the maximum actuation voltage should be smaller than the pull-in voltage, which is calculated to be around 7 volts from the analytical solutions in Figure 3.5. Before connecting the output actuation voltage to the micro-structure, conducting a frequency sweep to tabulate a frequency response curve is recommended. At electrical resonance, 217 kHz for the wire-bonded beam number 12, it is important to start with low input voltage at low frequency, i.e., 10 Hz, which is much smaller than that of the mechanical resonance frequency, 85 kHz. Once the micro-plate touches the bottom electrode, the plates may stick together permanently. It is important to understand that the electrical resonance frequency is for a carrier frequency that is generated by the RLC circuit, and the mechanical resonance frequency is when the displacement of the mechanical system is amplified the most. Table 4.3 shows a frequency sweep exam-

Table 4.3: Frequency sweep to find mechanical resonance frequency and gains

Frequency [kHz]	Input voltage [mV]	Output Voltage [mV]	Gain	Gain [dB]
10	100	100	1	0
100	112	144	1.286	2.18
110	108	200	1.852	5.35
150	108	576	5.333	14.5
200	118	1080	9.153	19.2
215	100	2080	20.8	26.4
219	84	3120	37.14	31.4
220	84	3000	35.71	31.1
221	88	2800	31.82	30.1
230	108	1000	9.26	19.3

ple recorded during the experiment. The bold-ed number is for the resonance frequency. Our RLC-driven electrostatic actuated MEMS demodulator requires less than 100 mV to provide over 3 volts actuation voltage, which is supplied to the MEMS paddle actuator by taking advantage of amplifications of 37 times the input voltage at its resonance. At 3 volts, according to Figure 3.5, the corresponding displacement is $0.03g_\circ$, where the initial gap is measured experimentally as $g_\circ 1.14\ \mu$m for the paddle actuator. There is room for increasing the input voltage to produce larger displacement, and thus a cleaner signal.

Type I MEMS AM demodulation result corresponding to signal at 500 Hz and 1 kHz are shown in Figure 4.13. The modulated signal's carrier frequency, f_c, is set at 355 kHz with $526mV_{pp}$. The actuation voltage is $11.48mV_{pp}$. Type II MEMS AM demodulation results ranging from 100 Hz to 1 kHz are shown in Figure 4.15, 4.16, and 4.17. Selected baseband frequencies at 100 Hz and 500 Hz and 1 kHz are tested. The gain has remained

AM

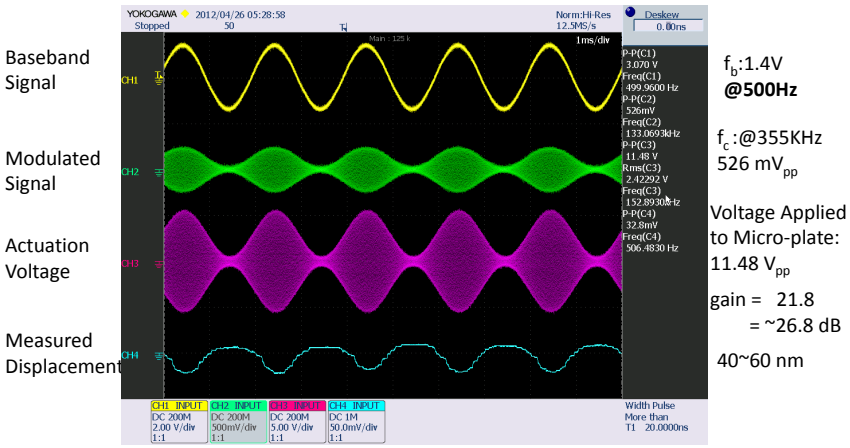

Figure 4.13: Type I MEMS AM demodulation result at 500 Hz

AM

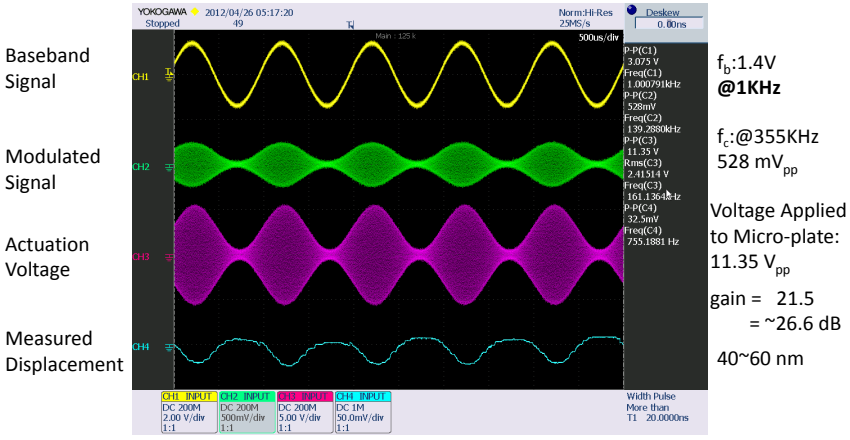

Figure 4.14: Type I MEMS AM demodulation result at 1 kHz

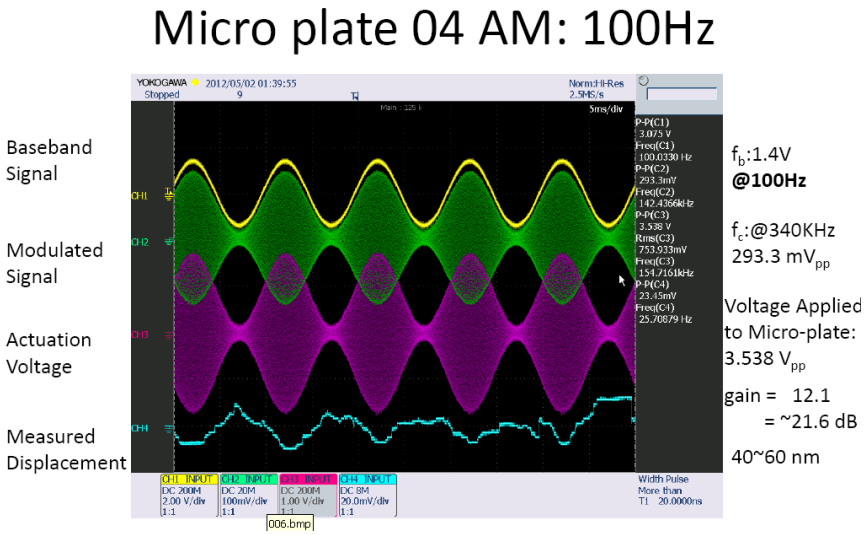

Figure 4.15: Type II MEMS AM demodulation result at 100 Hz

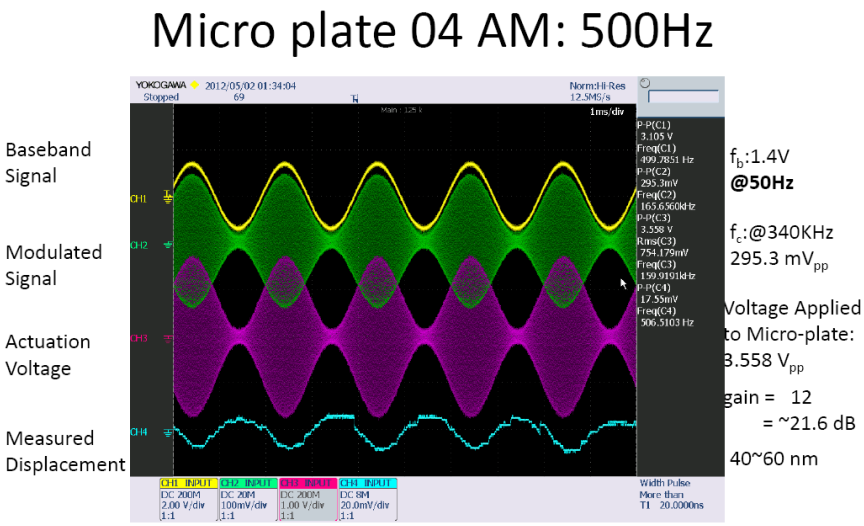

Figure 4.16: Type II MEMS AM demodulation result at 500 Hz

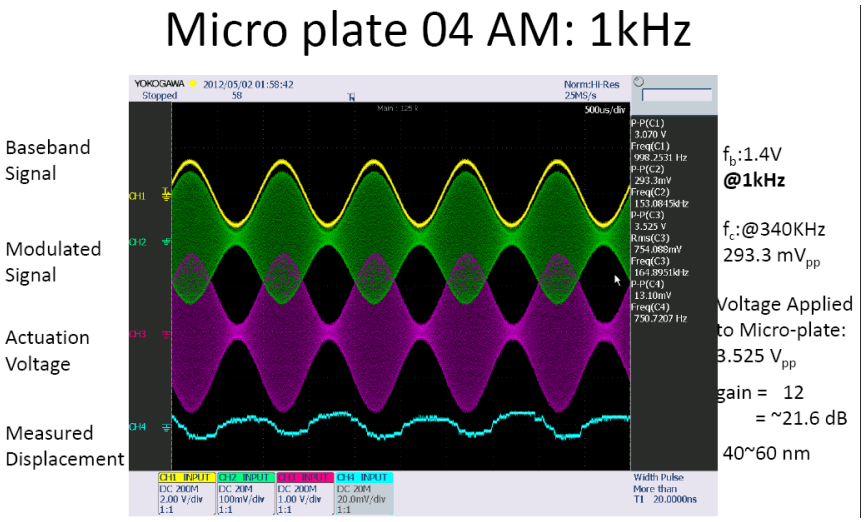

Figure 4.17: Type II MEMS AM demodulation result at 1 kHz

near constant: close to 27 dB for paddle actuator and 22 dB for the micro-plate actuator.

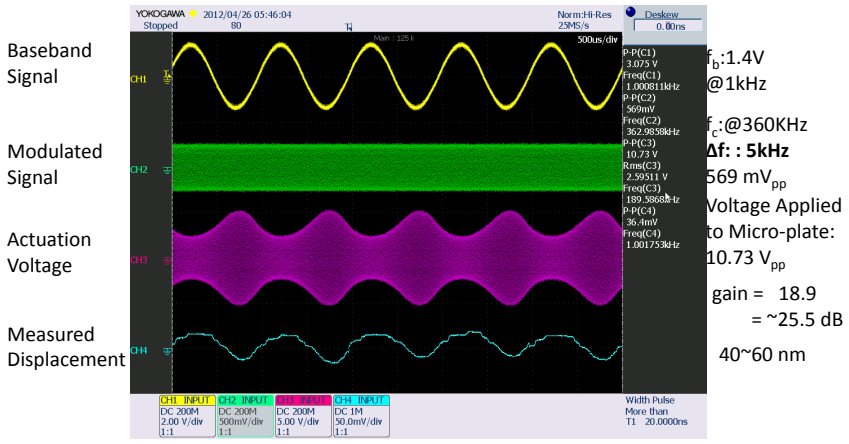

Figure 4.18: Type I MEMS FM demodulation with Δf of 5 kHz

4.3.2 FM Demodulation

The same baseband signal will be applied and mixed via a function generator capable of FM mixing. Optical detection of the displacement will provide data for a demodulated signal, which is the square root of the displacement. The BK 4086 AWG function generator is capable of FM modulation to produce an FM up to 20 MHz. It is not like an FM radio frequency but will be sufficient to conduct proof of concept experiments. Exactly the same micro-plate, Type I, MEMS electrostatic actuator that is used for AM demodulation is used for FM demodulation. Figure 4.18 shows results for the same 1 kHz baseband signal at 365 kHz with 10 kHz frequency deviation, Δf, and Figure 4.19 shows results for 1 kHz baseband signal at 360 kHz with 5kHz frequency deviation. The electrical resonance is at 355 kHz for both, and the gain is around 25 dB. The frequency deviation, Δf, affects the modulation index, h, h=Δf/f_m, where f_m is highest frequency component [25]. Thus shape of the actuation voltage appears to be sharp for the figure 4.19. In our case, h is

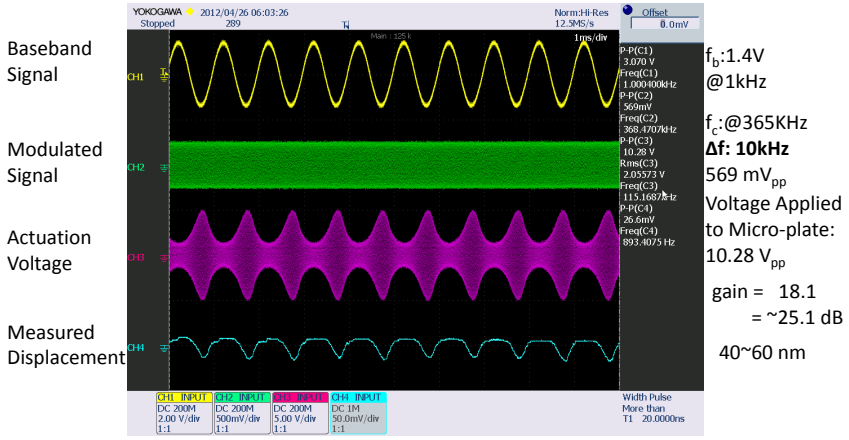

Figure 4.19: Type I MEMS FM demodulation with Δf of 10 kHz

0.0139 and 0.0274 respectively. These are a lot smaller than than one, thus the FM is narrow band system. According to Carson's rule [5], most of the power lies with in the bandwidth determined by twice of sum of the Δf and f_m. The larger the bandwidth the more immune to noise. Sharper the signal the more useful range of envelop there exists for the demodulator to distinguish the baseband signal.

Type II MEMS FM demodulation results ranging from 100Hz to 1kHz are shown in Figure 4.20, Figure 4.21, and Figure 4.22. All these results are showing the principle of the electrostatic MEMS actuator functioning as a demodulator when the device is implemented using the proposed MEMS demodulation architecture. Even for the baseband frequency, that were clearly detected as the measured displacement both by the vibrometer and by the phase detector circuit. The input voltage was around one volts peak-to-peak but after the resonance circuit where the micro-plate is part of the circuit component, the actuation voltage is amplified to 5.1 volts peak-to-peak with gain of five fold which is approximately

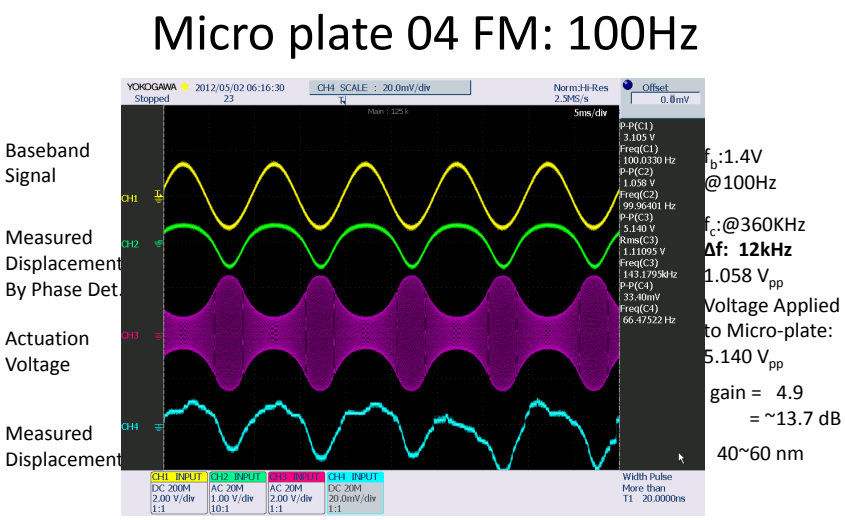

Figure 4.20: Type II MEMS FM demodulation at 100 Hz with Δf of 12 kHz

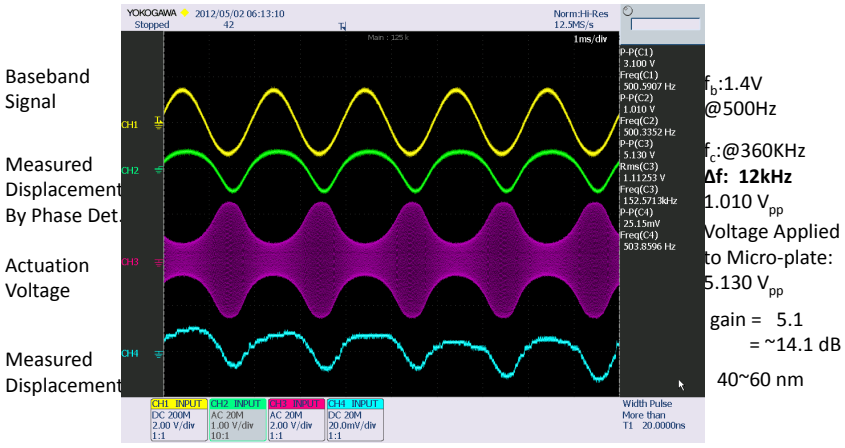

Figure 4.21: Type II MEMS FM demodulation at 500 Hz with Δf of 12 kHz

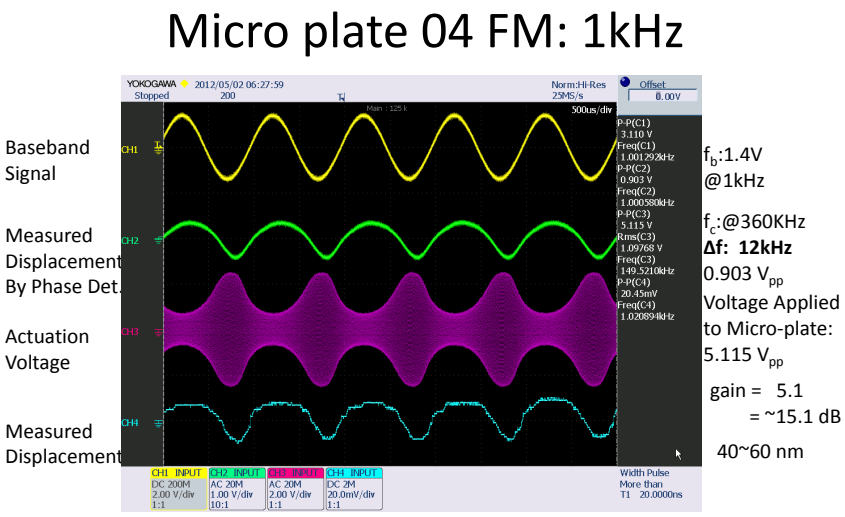

Figure 4.22: Type II MEMS FM demodulation at 1K Hz with Δf of 12 kHz

15.1 dB. The displacement is between 40 to 60 nm. Oscilloscope captures screen shot of the measurement data as shown in Figure 4.19. The modulated signal for FM contains higher frequency than that of the baseband signal thus the green line appears to be solid. However as soon as the actuation voltage is measured, the actual baseband signal is proportional to square root of the blue line at the bottom which is labeled as measured displacement of the MEMS electrostatic plate. Since we now know how the modulated signal appears to be at the low frequency display mode, in Figure 4.20 and there after, the channel is connected to the displacement measurement circuit using the phase detection method. Trends of the displacement signal shapes are quite close to each other for both method. The phase detector circuit is less pron to the the noise level.

4.4 Digital Demodulation Hardware Experiment

This section shows experimental results for our MEMS digital demodulator. ASK and FSK modulation schemes from a function generator is applied to the physically identical MEMS electrostatic actuator for digital demodulations. Nature of the vibrometer requires moving (vibrating) target to measure the displacement taking advantage of the Doppler's effect. For the digital demodulation experiment, vibrometer was not able to detect the on-off state of the plate. Essentially, the digital modulation is based on applying the actuation voltage for a certain period of time. Thus the micro-plate acts like a switch without actually making contact with the bottom electrode. Applied baseband signal is zero to five volts for both ASK and FSK. Again, exactly the same actuator was used for both types of modulation schemes.

$$s_b(t) = a_b \cos(2\pi f_b) + V_{dc} \tag{4.7}$$

Where the baseband signal $s_b(t)$ is expressed by $f_b = 100Hz$, DC offset voltage, $V_{dc} = 2.5$ volts, and amplitude of the baseband, $a_b = 2.5$.

4.4.1 ASK Demodulation

For type I actuator,

$$s_c(t) = a_c \cos(2\pi f_c) \tag{4.8}$$

The carrier signal, s_c consists of peak-to-peak input voltage of $a_c = 658mV_{pp}$, at the carrier frequency, $f_c = 355kHz$ which is electrical resonance of the electrostatic actuator. The applied voltage is only $2.143V_{pp}$ thus the gain is only two fold of 6 dB. When the baseband signal frequency is low (i.e. 100 Hz) the measured displacement takes more square shape following the actual baseband signal. However when the baseband frequency is increased to 1 kHz the measured displacement shows slightly distorted shape. Even though the

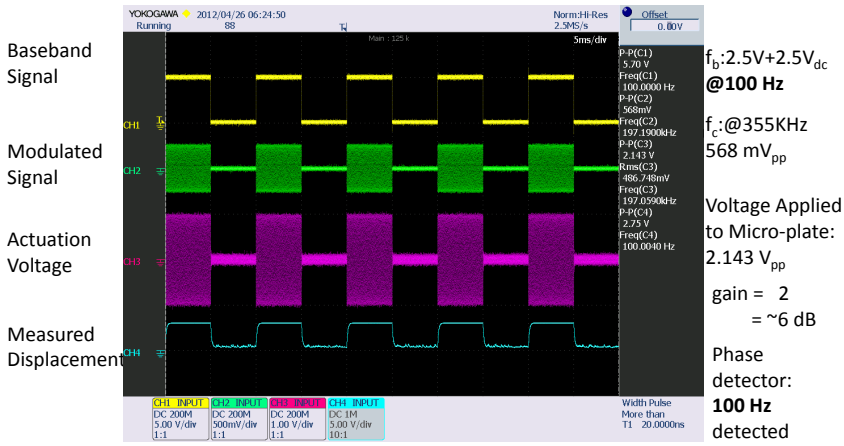

Figure 4.23: Type I MEMS ASK demodulation result at 100 Hz

actuation voltage shows rectangular like shape with sharp rises, the displacement can be characterized as a typical RC time delay behavior. Thus for the digital demodulation the MEMS electrostatic actuator will be more suitable for lower frequency. Determining the dynamic range of the useful spectrum by further investigation will be useful but for now, the phase detector is capable of detecting the baseband signal despite of the slight distortion to the shape of the detected signal. Figure 4.23 shows ASK MEMS digital demodulation results operating at 355 kHz when a baseband frequency of 100 Hz is applied. Although the gain is only about 6 dB, the phase detector clearly detects the 100 Hz demodulated signal. Figure 4.24 shows ASK MEMS digital demodulation results operating at 355 kHz when a baseband frequency of 500 Hz is applied. The gain is about 6 dB. Although the measured displacement starts to distorts a little bit due the phase detector clearly detects the 500 Hz demodulated signal. Similarly, Figure 4.25 shows ASK MEMS digital demodulation results operating at 355 kHz when a baseband frequency of 1 KHz is applied.

ASK

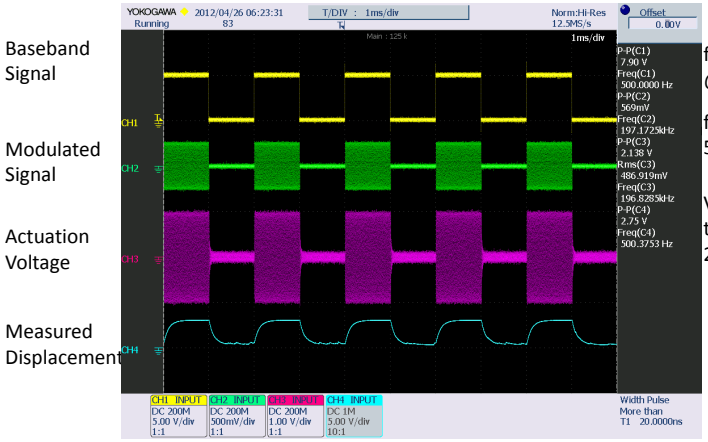

Figure 4.24: Type I MEMS ASK demodulation result at 500 Hz

ASK

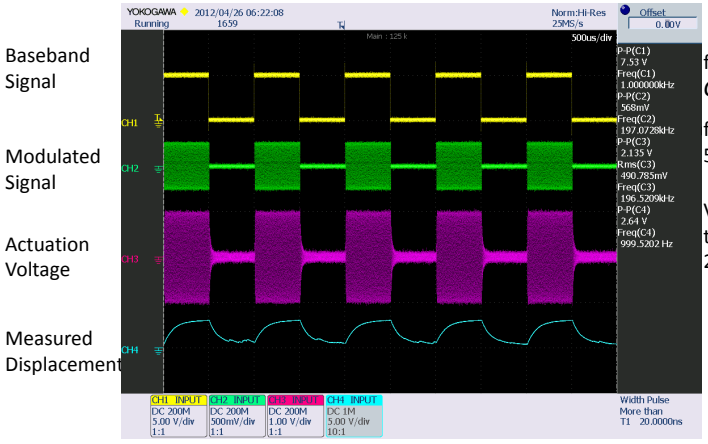

Figure 4.25: Type I MEMS ASK demodulation result at 1 kHz

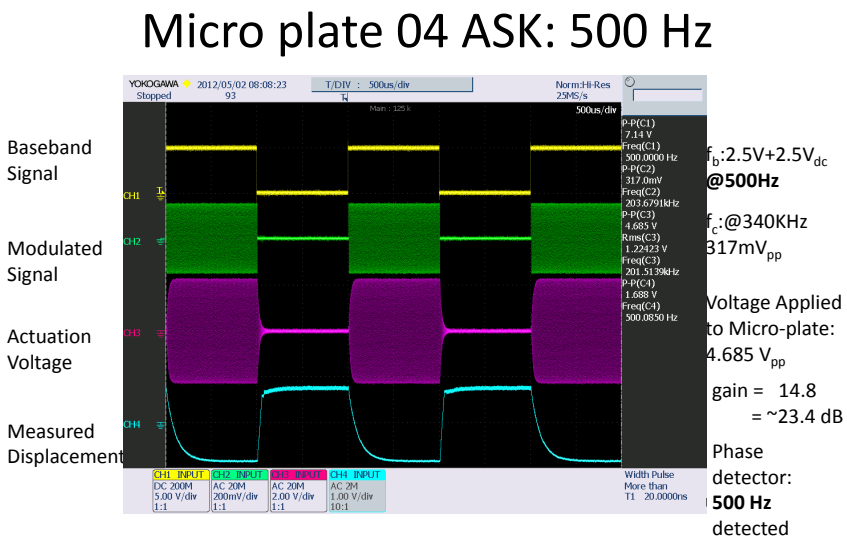

Figure 4.26: Type II MEMS ASK demodulation result at 500Hz

The gain is about 6 dB. Although the measured displacement by phase detector is further distorted, the oscilloscope captures the 1 KHz demodulated signal that the phase detector has detected. Micro-plate 04 is the type II MEMS actuators. Its ASK demodulation results of 500Hz and 1kHz are shown in Figure 4.26 and Figure 4.27. Compare to the type I MEMS ASK demodulation, the gain is significantly higher by 17.4 dB. The sole purpose of testing type II is to prove that the demodulation architecture using MEMS electrostatic actuator as demodulator works for various types of electrostatic actuator. Thus detailed characterization, analysis, and optimization are not pursued for this sets of experiment.

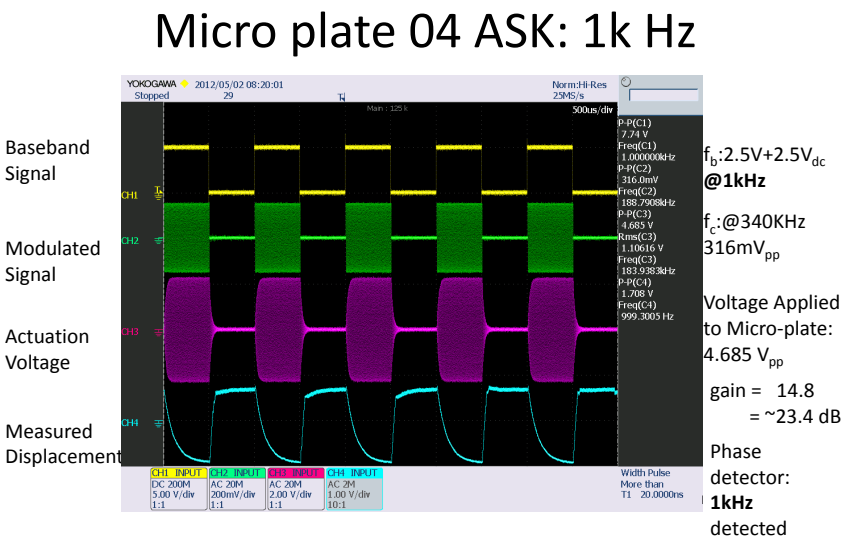

Figure 4.27: Type II MEMS ASK demodulation result at 1KHz

4.4.2 FSK Demodulation

Figure 4.28 shows FSK MEMS digital demodulation results operating at 355 kHz and 155 kHz when a baseband frequency of 100 Hz is applied. Although the gain is only about 12 dB, the phase detector clearly detects the 100 Hz demodulated signal. Figure 4.29 shows FSK MEMS digital demodulation results operating at 355 kHz and 155 kHz when a baseband frequency of 500 Hz is applied. The gain is about 12 dB. Although the measured displacement starts to distorts a little bit due the phase detector again it clearly detects the 500 Hz demodulated signal. Similarly, Figure 4.30 shows FSK MEMS digital demodulation results operating at 355 kHz and 155 kHz when a baseband frequency of 1 KHz is applied. The gain is about 12 dB. Although the measured displacement by a phase detector is further distorted, the oscilloscope captures the 1 KHz demodulated signal what the phase detector has detected. Type II MEMS FSK, labeled Micro-plate 04 FSK, and its demodulation experimental results of 500Hz and 1kHz are shown in Figure 4.31 and Figure 4.32. Because

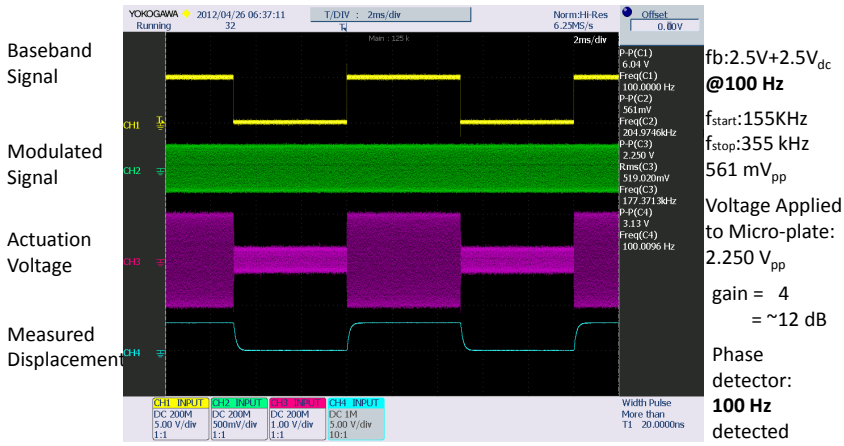

Figure 4.28: Type I MEMS FSK demodulation result at 100 Hz

the the frequency difference is only 100 kHz apart for type I, the actuation voltage at zero is not quite zero. However for the type II, the difference between the two signal is 339.9 kHz. Thus the actuation voltage at the electrical resonance 340 kHz is at the maximum achieving the gain on 23.5dB while at zero almost no actuation voltage is applied to the micro-plate. The wavy green lines are artifact from the digital oscilloscope due to its own sampling limitation, but assume the wavy lines are flat at zero. Again, at 1 kHz the measured displacement shows similar characteristic as what was observed in ASK experimental results. Also the overall results show similar trend of the flat top following the baseband signal more closely at lower frequency. MEMS demodulator may not be the most ideal and optimal case for the FSK, but the studied MEMS demodulator architecture works for all modulation schemes tested. The standalone fully functioning device were able to recover the baseband signal under any of these (AM FM ASK FSK) modulations scheme using exactly same electrostatic actuator without further design optimization.

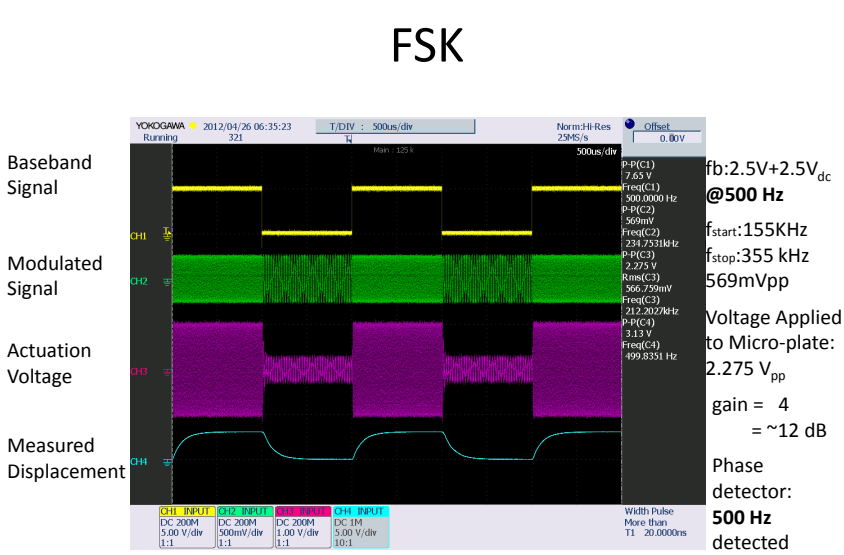

Figure 4.29: Type I MEMS FSK demodulation result at 500 Hz

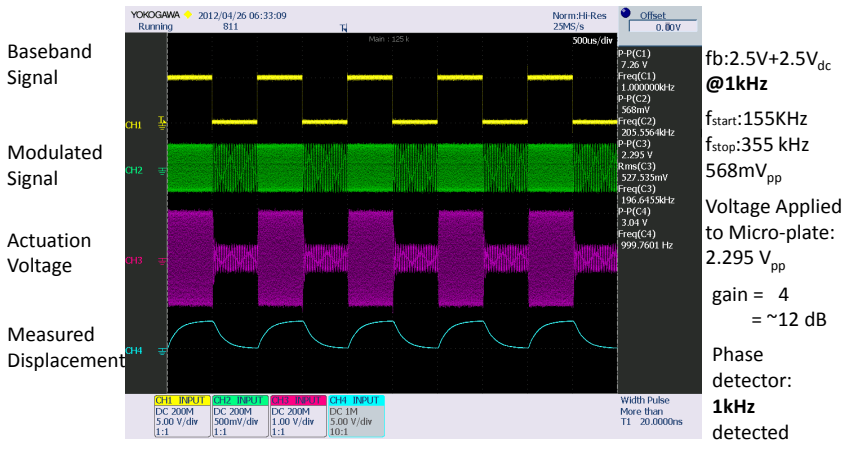

Figure 4.30: Type I MEMS FSK demodulation result at 1 kHz

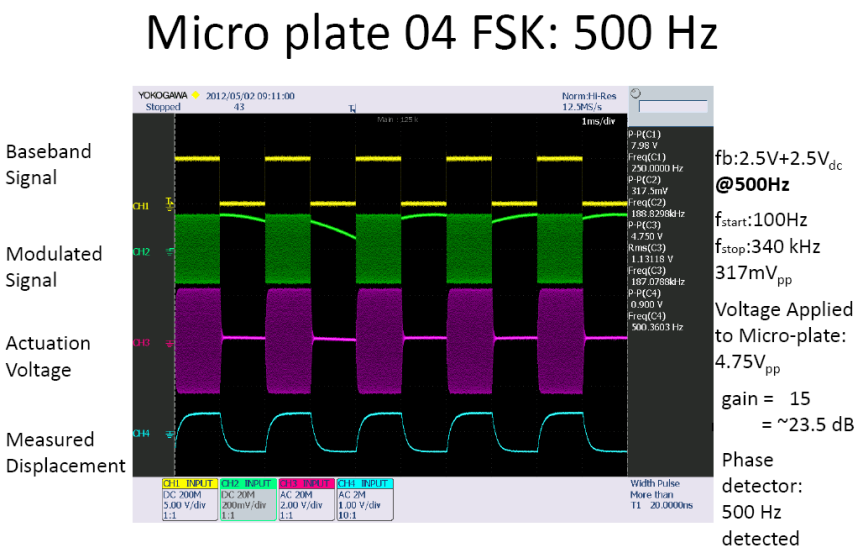

Figure 4.31: Type II MEMS FSK demodulation result at 500Hz

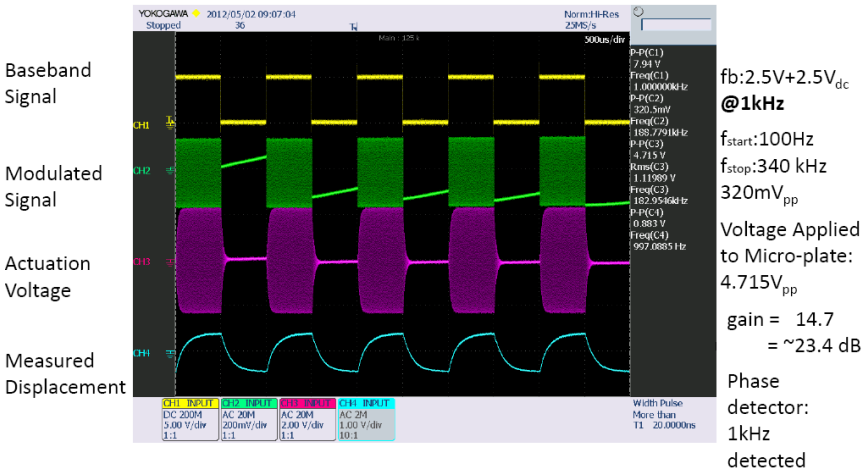

Figure 4.32: Type II MEMS FSK demodulation result at 1KHz

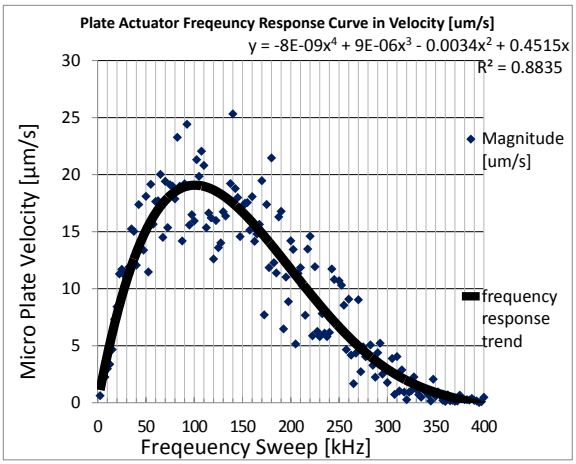

Figure 4.33: Type II Plate Actuator Frequency Response Curve using Velocity Dectotor

4.5 MEMS Demodulation Limitation

Limitation of MEMS Demodulation is described in this section. Analysis is carried out to find the natural frequency based on the experimental results. Figure 4.33 is collection of FFT data during a frequency sweep. The graph peak at 142.5 kHz although the fourth order curve fitting graph suggests the peak around 100 kHz. The plate actuator's velocity is measured in μm per seconds. The main purpose of the test is to find the natural frequency of the plate used for demodulation experiment. Vibrometer's displacement decoder DD200 is limited to detecting 25 kHz the maximum. Thus the vibrometer's velocity decoder VD-02 is used for the measurement. VD-02 is capable of measuring 5mm/s/V up to the band width of 250 kHz. For the type II, the centre mechanical resonance was near 140 based on finding the peak value by eyeballing. For this particular electrostatic actuator, the upper limit of the baseband signal can be set at one-third of the peak at 30 to 40 kHz which is still above the human hearing range of 20 kHz.

Chapter 5

Conclusions

The first chapter provided analytical model for a MEMS paddle structure electrostatic actuator. The normalized displacement and the normalized voltage curve plot in Figure 3.4 allows numerical simulations for similar micro paddle structures. Table (3.1) and (3.2) contain every single parameters that are required to build the numerical model to exploit the proposed electrostatic MEMS demodulator's ability to double as an AM demodulator and an FM demodulator as well as ASK and FSK digital demodulators that can be used in a single receiver. The dynamic range of the device and its limitations need to be identified. The component should be compatible with existing receivers. Although initially only the baseband frequency of 100 Hz and 200 Hz were presented experimentally, nonetheless the MEMS demodulator has successfully extracted the two specific baseband frequency. As long as the baseband frequency's range is less than the natural frequency of the actuator MEMS electrostatic actuator based demodulation architecture works. Numerical simulations and experiment showed that the shape of the displacement signal follows the envelope of the modulated signal input. Total capacitance changes as the displacement changes when the modulated signal is applied. The electrical resonant frequency depends on resistance and inductance thus it does not move away from the predefined carrier frequency. The

mechanical response to the modulated signal consisting of two frequency components tend to follow the slower motion (thus low frequency); but the modulated signal input is not capable of following the high frequency that is beyond the natural frequency of the electrostatic actuator. Thus, the displacement follows the envelop of the modulated signal. For now, the displacement is measured optically by vibrometer and by a fully functioning demodulator device. This MEMS demodulator not only replaces the current demodulators composed of mixers and oscillators for downconverting input signals, and but also filters out high electrical frequency noise. The physical displacement of the micro-plate is represented in terms of voltage output that can be further process by square-rooting to extract true baseband signal by measuring the phase difference near the electrical resonant. MEMS FM demodulator can be used in a single receiver. Numerical experiment showed that the actuation voltage stays constant without drastic decay. Towards that end, the dynamic range of the device and its limitations need to be identified in detail. The MEMS demodulator is compatible with existing receivers. Different types of micro-actuators have their unique characteristics. Further simulations and experiments are planned to optimize the dimensions of the micro-actuator to the point where it will run at the target carrier frequencies of actual radio stations, such as 680 kHz or 1440 kHz.

Bibliography

[1] Vito Giannini, Jan Craninckx, and Andrea Baschirotto. *Digitally-assisted analog and RF CMOS circuit design for software-defined radio*. Springer, New York, c2011 edition, 2011. 2

[2] Vito Giannini, Jan Craninckx, and Andrea Baschirotto. *Baseband Analog Circuits for Software Defined Radio*. Springer, Dordrecht, c2008 edition, 2008. 3

[3] S. Park and E. Abedel-Rhman. Low voltage electrostatic actuation and displacement measurement through resonant drive circuit. In *Proceedings of the ASME 2012 International Design Engineering Technical Conference and Computers and Information in Engineering Conference*, 2012. 3, 54

[4] B. Razavi. Design considerations for direct-conversion receivers. *IEEE Transactions on Circuits and Systems II: Analog and Digital Signal Processing*, 44(6):428–435, 06 1997. 7, 11

[5] John G. Proakis and Masoud. Salehi. *Digital Communications*. McGraw-Hill Higher Education, Boston, 5th ed edition, 2008. 10, 70

[6] C.T.C. Nguyen. Micromechanical circuits for wireless communications. In *Proceeding of the 30th European Solid-State Device Research Conference*, pages 2–12, 2000. x, 13, 14

[7] D. E. Anagnostou, Guizhen Zheng, M. T. Chryssomallis, J. C. Lyke, G. E. Ponchak, J. Papapolymerou, and C. G. Christodoulou. Design, fabrication, and measurements of an rf-mems-based self-similar reconfigurable antenna. *IEEE Transactions on Antennas and Propagation*, 54(2):422–432, 2006. 15

[8] E. R. Brown. Rf-mems switches for reconfigurable integrated circuits. *Microwave Theory and Techniques, IEEE Transactions on*, 46(11):1868–1880, 1998. 15

[9] G. M. Rebeiz and J. B. Muldavin. Rf mems switches and switch circuits. *IEEE Microwave Magazine*, 2(4):59–71, 2001. 14, 15

[10] K. Entesari, K. Obeidat, A. R. Brown, and G. M. Rebeiz. A 2575-mhz rf mems tunable filter. *Microwave Theory and Techniques, IEEE Transactions on*, 55(11):2399–2405, 2007. 15

[11] J. F. Carpentier, A. Cathelin, C. Tilhac, P. Garcia, P. Persechini, P. Conti, P. Ancey, G. Bouche, G. Caruyer, D. Belot, C. Arnaud, C. Billard, G. Parat, J. B. David, P. Vincent, M. A. Dubois, and C. Enz. A sige:c bicmos wcdma zero-if rf front-end using an above-ic baw filter. In *IEEE International Solid-State Circuits Conference*, volume 1, pages 394–395, 2005. 15

[12] M. Koskenvuori and I. Tittonen. Towards micromechanical radio: Overtone excitations of a microresonator through the nonlinearities of the second and third order. *Journal of Microelectromechanical Systems*, 17(2):363–369, 2008. 14, 15, 19, 22, 24

[13] K. E. Wojciechowski, R. H. Olsson, M. S. Baker, and J. W. Wittwer. Low vibration sensitivity mems resonators. In *Frequency Control Symposium, 2007 Joint with the 21st European Frequency and Time Forum. IEEE International*, pages 1220–1224, 2007. 14, 15

[14] G. M. Rebeiz. Rf mems for low power wireless communications. In *International Conference on MEMS, NANO and Smart Systems*, page 327, 2005. 14

[15] Gabriel M. Rebeiz. *RF MEMS : theory, design, and technology*. Wiley-Interscience, Hoboken, N.J., 2003. 14

[16] E. R. Brown. Rf mems switches for reconfigurable integrated circuits. In *Microwave Theory and Techniques IEEE Transactions*, 1998. 14

[17] A. Uranga, J. Verd, J. L. Lopez, J. Teva, G. Abadal, F. Torres, J. Esteve, F. Perez-Murano, and N. Barniol. Fully integrated mixler based on vhf cmos-mems clamped-clamped beam resonator. *Electronics Letters*, 43(8):452–454, APRIL 2007. 16

[18] Kun Wang, Ark-Chew Wong, and C. T.-C. Nguyen. Vhf free-free beam high-q micromechanical resonators. *Journal of Microelectromechanical Systems*, 9(3):347–360, 2000. 16

[19] Ark-Chew Wong and C. T. C Nguyen. Micromechanical mixer-filters "mixlers". *Microelectromechanical Systems, Journal of*, 13(1):100–112, 2004. x, 17, 18, 22, 24

[20] M. KosIenvuori, I. Tittonen, and A. Alastalo. Ghz-range fsk-reception with microelectromechanical resonators. *SENSORS AND ACTUATORS A-PHYSICAL*, 147(1):358–358, 2008. 19, 22, 24

[21] M. Koskenvuori and I. Tittonen. Parametrically amplified microelectromechanical mixer. In *21st International Conference on Micro Electro Mechanical Systems, MEMS 2008 Tucson*, pages 1044–1047. IEEE, 2008. 19, 22, 24

[22] M. Koskenvuori and I. Tittonen. Improvement of the conversion performance of a resonating multimode microelectromechanical mixer-filter through parametric amplification. *IEEE Electron Device Letters*, 28(11):970–972, 2007. 19, 22, 24

[23] R. B. Reichenbach, M. Zalalutdinov, K. L. Aubin, R. Rand, B. H. Houston, J. M. Parpia, and H. G. Craighead. Third-order intermodulation in a micromechanical thermal mixer. *Journal of Microelectromechanical Systems*, 14(6):1244–1252, 2005. x, 19, 20, 23, 24

[24] R B Reichenbach, M Zalalutdinov, J M Parpia, and H G Craighead. Rf mems oscillator with integrated resistive transduction. *IEEE ELECTRON DEVICE LETTERS*, 27(10):805–807, 2006. x, 20, 21, 23, 24

[25] E. Mastropaolo, I. Gual, and R. Cheung. Silicon carbide electrothermal mixer-filters. *Electronics Letters*, 46(1):62–63, 2010. x, 21, 22, 23, 24, 69

[26] Larry K. Baxter. *Capacitive Sensors - Design and Applications*. Wiley-IEEE Press, 1997. 23

[27] G. Gautschi. *Piezoelectric sensors : force, strain, pressure, acceleration and acoustic emission sensors, materials and amplifiers*. Springer, Berlin ; New York, 2002. 23

[28] Seung-Bok Choi and Young-Min Han. *Piezoelectric actuators : control applications of smart materials*. CRC Press, Boca Raton, FL., 2010. 23

[29] Stanley Kon. High resolution mems strain sensors for vibration detection on hard disk drive instrumented suspensions, 2007. SO: Dissertation Abstracts International. Vol. 68, no. 8. 2007. 23

[30] A. A. Barlian, W. T Park, J. R. Mallon, A. J. Rastegar, and B. L. Pruitt. Review: Semiconductor piezoresistance for microsystems. *Proceedings of the IEEE*, 97(3):513–552, 2009. 23

[31] Mahmoud Khater. *Use of Instabilities in Electrostatic Micro-electro-mechanical Systems for Actuation and Sensing*. PhD thesis, University of Waterloo, Waterloo, Ont., 2011. 25, 37

[32] D. Elata. On the static and dynamic response of electrostatic actuators. In *Bulletin of the Polish Academy of Science Technical Sciences*, volume 53, 2005. 28

[33] J. Carter, A. Cowen, B. Hardy, R. Mahadevan, M. Stonefield, and S. Wilcenski. *PolyMUMPs Design Handbook, Revision 11.* MEMSCAP Inc., 2005. 39

[34] Shahrzad Towfighian. *A Large-Stroke Electrostatic Micro-Actuator.* PhD thesis, University of Waterloo, Waterloo, Ont., 2010. 43

[35] M.E. Khater, E.M. Abdel-Rahman, and A.H. Nayfeh. A mass sensing technique for electrostatically-actuated mems. In *ASME IDETC*, pages DETC2009–87551. ASME, September 2009. 43

[36] Using Simulink. *Dynamic System Simulation for MATLAB.* The Math Works Inc., USA, ver3 edition, 1999. 44

[37] Sangtak Park. *Low Voltage Electrostatic Actuation and Displacement Measurement through Resonant Drive Circuit.* PhD thesis, University of Waterloo, Waterloo, Ont., 2011. 52

[38] A. T. Alastalo, M. Koskenvuori, H. Seppa, and J. Dekker. A micromechanical resonating rf mixer. In *34th European Microwave Conference*, volume 3, pages 1297–1300, 2004.

[39] J. J. Carr. *RF components and circuits.* Newnes, Oxford, 1st ed edition, 2002.

[40] J. R. Clark, F. D. Bannon III, Ark-Chew Wong, and C. T. C Nguyen. Parallel-resonator hf micromechanical bandpass filters. In *Solid State Sensors and Actuators, 1997. TRANSDUCERS '97 Chicago., 1997 International Conference on*, volume 2, pages 1161–1164, 1997.

[41] B. E. DeMartini, J. F. Rhoads, K. L. Turner, S. W. Shaw, and J. Moehlis. Linear and nonlinear tuning of parametrically excited mems oscillators. *Microelectromechanical Systems, Journal of*, 16(2):310–318, 2007.

[42] Robert C. (Robert Clyde) Dixon. *Radio receiver design*. Marcel Dekker, New York, 1998.

[43] J. H. Ginsberg. *Mechanical and structural vibrations : theory and applications*. Wiley, New York, 1st ed edition, 2001.

[44] A. K. Ismail, J. S. Burdess, A. J. Harris, C. J. McNeil, J. Hedley, S. C. Chang, and G. Suarez. The principle of a mems circular diaphragm mass sensor. *Journal of Micromechanics and Microengineering*, 16(8):1487–1493, 08 2006.

[45] Gregory T. A. Kovacs. *Micromachined transducers sourcebook*. WCB/McGraw-Hill, Boston, 1998.

[46] S. Lucyszyn. Review of radio frequency microelectromechanical systems technology. *Science, Measurement and Technology, IEE Proceedings* -, 151(2):93–103, 2004.

[47] Devendra Misra. *Radio-frequency and microwave communication circuits : analysis and design*. Wiley, New York ; Chichester [England], 2001.

[48] M. Motiee, R. R. Mansour, and A. Khajepour. Micromechanical resonators and filters for microelectromechanical system applications. *Journal of Vacuum Science & Technology B*, 24(6):2499–2508, 11 2006.

[49] R. B. Reichenbach, K. L. Aubin, M. Zalalutdinov, J. M. Parpia, and H. G. Craighead. A mems rf phase and frequency modulator. In *Solid-State Sensors, Actuators and Microsystems, 2005. Digest of Technical Papers. TRANSDUCERS '05. The 13th International Conference on*, volume 1, pages 1059–1062, 2005.

[50] R. B. Reichenbach, M. K. Zalaludinov, K. L. Aubin, D. A. Czaplewski, B. Ilic, B. H. Houston, H. G. Craighead, and J. M. Parpia. Resistively actuated micromechanical dome resonators. In Siegfried W. Janson and Albert K. Henning, editors, *MEMS/MOEMS Components and Their Applications*, volume 5344, pages 51–58. SPIE, January 2004.

[51] J. Yeager and M. A. Hrusch-Tupta. *Low level measurements : precision DC current, voltage, and resistance measurements*. Keithley Instruments, Cleveland, OH, 5th ed edition, 1998.